PAPER • OPEN ACCESS

Model-based investigations of ferroelectric energy harvesting with regard to an improvement of life span and operability

To cite this article: Andreas Warkentin *et al* 2023 *Smart Mater. Struct.* **32** 035028

Model-based investigations of ferroelectric energy harvesting with regard to an improvement of life span and operability

Andreas Warkentin*, Lennart Behlen and Andreas Ricoeur

University of Kassel, Institute of Mechanics, Kassel, Germany

E-mail: warkentin@uni-kassel.de

Abstract

A new ferroelectric energy harvesting concept is investigated theoretically, based on a thermo-electromechanical multiscale constitutive framework in connection with the so-called condensed method. Taking advantage of comparatively large changes of strain and polarization due to domain switching, the electric output is higher compared to what is commonly known as piezoelectric energy harvesting. Dissipative self-heating and augmented damage accumulation, on the other hand, may impede the operability of the harvesting device, in particular if tensile stress is required for depolarization, as suggested by recent works. The new harvesting cycle thus dispenses with tensile stresses and instead exploits the potential of existing residual stresses. It is further investigated to which extent a bias field, commonly applied to support repolarization as an important stage of the cycle, can be omitted, saving considerable effort on the technical implementation. Process parameters are obtained from various simulations by pareto-optimization, considering, inter alia, the effect of ambient temperature.

Keywords: ferroelectrics, piezoelectrics, self-heating, energy conversion, cyclic process, multiscale

(Some figures may appear in colour only in the online journal)

1. Introduction

Energy harvesting concepts target the exploitation of naturally available energy, mostly mechanical or thermal, in terms of conversion into electrical energy. Since the sources, e.g. environmentally induced mechanical vibrations or temperature changes, are available for free, the efficiency of energy conversion is not a paramount issue. Rather, the figures of merit must be a measure of the best possible use of the available ambient power. In recent years, concepts of ferroelectric energy harvesting have been investigated in this regard [1–8], having a focus on vibrational mechanical energy exploitation. In contrast to what is today known as piezoelectric energy harvesting [9–12], having emerged around the turn of the millennium, the switching of lattice cells and domain wall motion, respectively, give rise to a larger electric output processed from an augmented mechanical input. Issues of ferroelectric harvesters, on the other hand, are dissipative self-heating and mechanical degradation of the essentially brittle functional materials involved.

In a recent work of the authors [6], a ferroelectric harvesting cycle, previously introduced by Kang and Huber [5], has been investigated theoretically, based on a multiscale constitutive
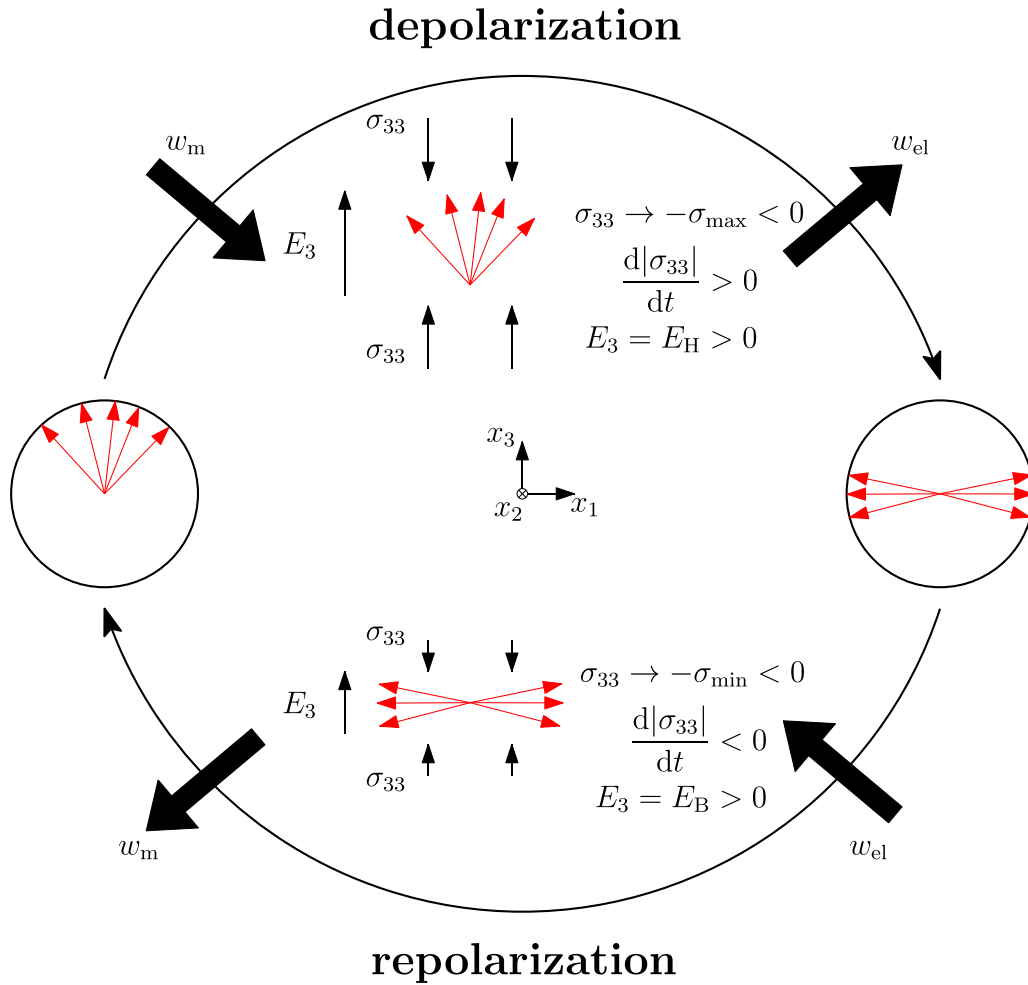
Figure 1. Schematic of the new harvesting cycle illustrating exchange of electrical and mechanical works, operating stress and electric field parameters and polarization states.

framework of polycrystalline ferroelectrics in connection with the so-called condensed method (CM). Based on numerical simulations and nonlinear optimization with regard to figures of merit, suitable mechanical and electric process parameters were identified, and an extended harvesting cycle was introduced by means of increased degrees of freedom. One fundamental drawback of the concept is that tensile stress is induced for depolarization along with a perpendicular electric harvesting field required for the electric power output. This significantly promotes the formation and growth of cracks and thus reduces the life span and finally the operability of the harvesting device.

In the work at hand, a modified cyclic process that does not rely on any tensile stress is being investigated. Figure 1 illustrates the procedure of converting mechanical work input $w_{\mathrm{m}} > 0$ into electric output $w_{\mathrm{el}} < 0$ with electric harvesting (E_{H}) and bias (E_{B}) fields being involved. The latter, being of comparatively small magnitude, i.e. $E_{\mathrm{B}} \ll E_{\mathrm{H}}$, supports the repolarization during compressive stress relief $(w_{\mathrm{m}} < 0)$, while the harvesting field is active during the depolarization period. It simulates the effect of the impedance of an external electric circuit [7], e.g. for charging a battery, and is thus not controlled directly in technical applications. The bias field, first

introduced in ferroelectric energy harvesting by Wang *et al* [3, 4], on the other hand, is imposed by a control unit. The red arrows in figure 1 depict the states of polarization at different stages of the cycle. Compared to the concept of [5, 6], electric and mechanical loads now act collinearly and the depolarization is driven by residual stress originating from incompatibilities of strain and inhomogeneous material properties on the level of the polycrystalline mesostructure.

This crucial feature is illustrated exemplarily in figure 2, where the irreversible switching-related part of the polarization is plotted versus the external electric load. Two cases are investigated, i.e. a single crystal and a polycrystalline ferroelectric. The theoretical background of the calculations will be outlined in the following sections, material parameters are those of barium titanate (BT) [14]. While the single crystal hysteresis resembles a rectangle with identical loading and unloading paths above the coercive field of $0.2\,\mathrm{kV\,mm^{-1}}$, the polycrystalline behavior exhibits a distinct drop in polarization ΔP^{irr} at unloading, depicted in the enlarged detail. The residual stresses further impede 90°-switching in the polarization process, which manifests itself in the lower magnitude of maximum polarization $P^{\mathrm{irr}}_{\mathrm{max}}$ for the polycrystalline material. Although omitting tensile loads is in principle a compromise
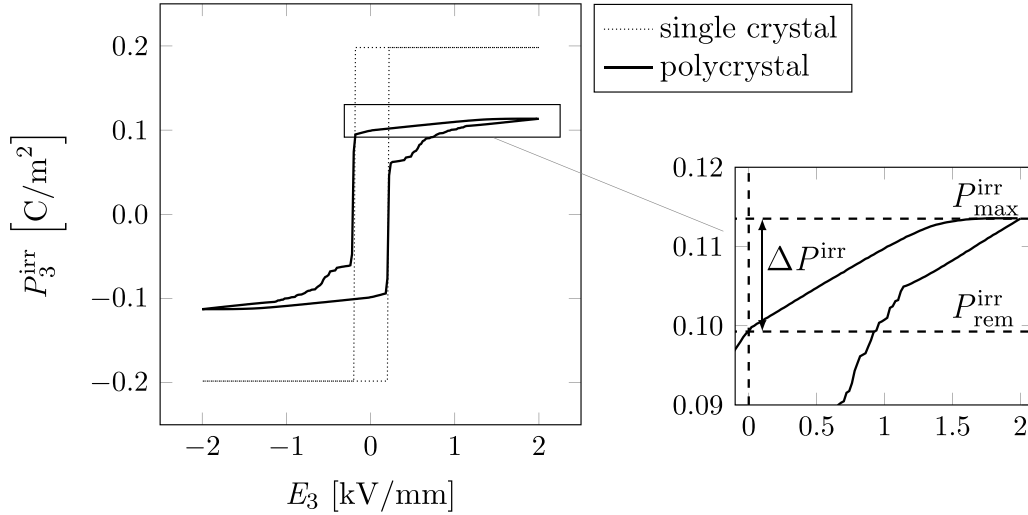
Figure 2. Irreversible polarization vs. electric field hysteresis loops from simulations of single- and polycrystalline barium titanate loaded bipolarly with $\pm 10 E_{\mathrm{C}} = \pm 2\,\mathrm{kV}\,\mathrm{mm}^{-1}$; enlarged section emphasizes the drop of polarization ΔP^{irr} at unloading.
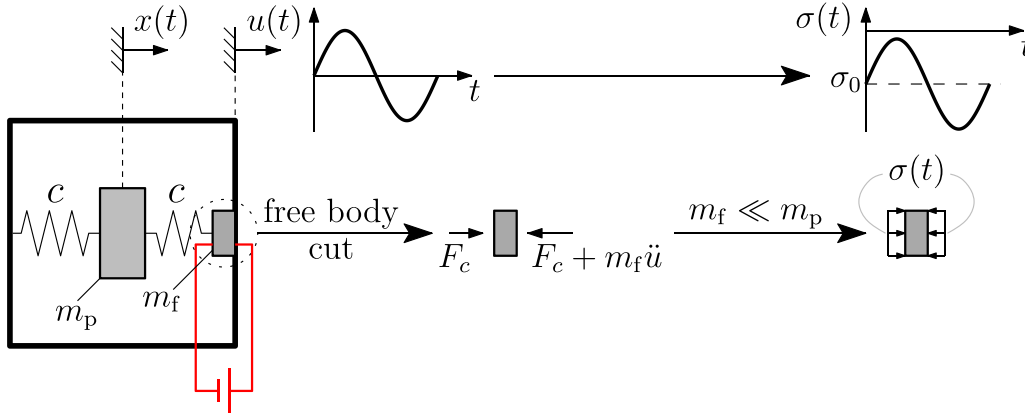

Figure 3. Engineering implementation of the new ferroelectric harvesting cycle in the style of Williams and Yates [13] with springs c, energy storing proof mass m_{p} and harvester m_{f}, deflected by $x(t)$ and $u(t)$, respectively, in mechanically excited oscillation.

at the expense of electric power output, the simulations will show that the loss is not substantial.

In figures 3 and 4, two possibilities for technical implementation of the new harvesting concept are illustrated, the first relying on a mass-spring system, the second exploiting vibrations of a beam-like structure. In both cases, solely compressive stress is induced, introducing the definitions

$$\sigma_{\min} = \min|\sigma(t)|, \quad \sigma_{\max} = \max|\sigma(t)|,$$
$$\sigma_0 = \left| \frac{1}{T} \int_0^T \sigma(t)\mathrm{d}t \right|. \tag{1}$$

In the idea of figure 4(a) compressive pre-stress, accomplished either by oversize of the harvester or a pair of springs, guarantees compression in the tensile stage of beam deflection and furthermore allows the targeted setting of the mean stress σ_0. The fact that in figure 4 the grey area representing the harvester might give the impression that a bending takes place there is due to the exaggerated depiction, whereby the harvester is in reality significantly thinner than the substrate.

In this work, a theoretical framework, including thermodynamical considerations regarding the non-equilibrium multiscale constitutive behavior and cyclic electro-thermomechanical processes, is outlined first. In contrast to [6], aspects of dissipative self-heating, thermo-electromechanical coupling and the effect of evolution of material coefficients due to domain wall motion are taken into account. Fundamentals of the scale-bridging approach, denoted as CM, are depicted in brief and can be further studied, e.g. in [14–16]. Simulations confirm the feasibility of the new harvesting concept and pareto-optimization reveals appropriate process parameters in light of competing targets of efficiency of energy conversion and maximal electric power output. The influence of ambient temperature on the figures of merit is investigated just as the heat production per cycle as a measure of domain activity and eventually of potential damage accumulation. To avoid the technical effort of controlling a bias field, the latter is finally omitted in simulations, in order to study its significance in respect of the repolarization process as well as its impact on the figures of merit.
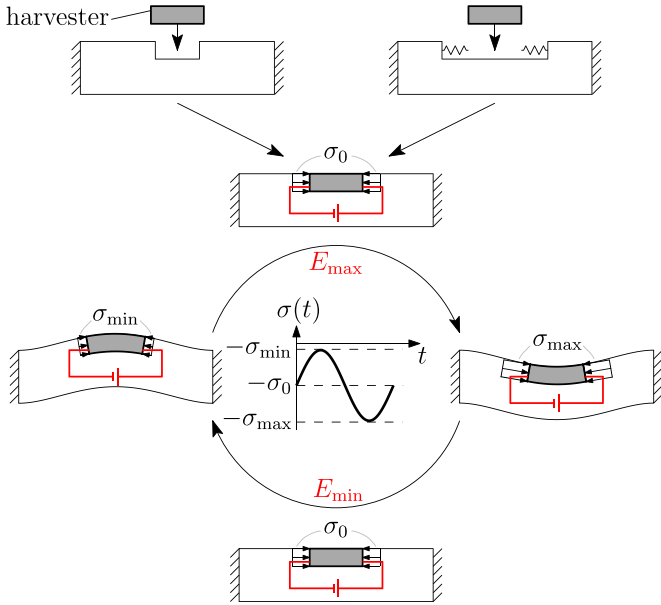
Figure 4. Engineering implementation of the new ferroelectric harvesting cycle exploiting compressive stress $\sigma(t)$ by means of vibration of a beam-like structure.

2. Theoretical framework

2.1. Thermodynamics of irreversible thermoelectromechanical processes

Stating the conservation of energy, the 1st law of thermodynamics for closed systems at rest identifies the sum of total work done on a system and heat exchange across its boundary with a change in internal energy. Interpretation of this fundamental principle in the framework of continuum mechanics presumes mechanically quasistatic scenarios, ending up with a local balance of power reading

$$\dot{u} = \dot{w} + \dot{q}, \tag{2}$$

where a dot represents the material time derivative, $\dot{q}$ is the volume specific heat flux, and u and w denote the volume specific internal energy and total work, respectively. Application of infinitesimal strain theory, suitable for brittle ferroelectrics, renders a further distinction between current and initial configuration obsolete. Additionally, neglecting magnetic quantities as well as free electric charges and currents within the scope of electrostatic considerations in dielectric materials allows for a specification of the right-hand side of equation (2) in terms of [17]

$$\dot{w} = \dot{w}^{\text{rev}} + \dot{w}^{\text{irr}} = \sigma_{ij}\dot{\varepsilon}_{ij} + E_i\dot{D}_i, \tag{3}$$

$$\dot{q} = \rho r - q_{i,i}, \tag{4}$$

where an underlying Cartesian coordinate system is implicitly assumed from this point on, Einstein summation convention is applied to repeated indices and a comma refers to partial differentiation with respect to the corresponding coordinate. In equations (3) and (4), σ_{ij} and ε_{ij} are the Cauchy stress- and

strain tensor, respectively, E_i and D_i are the electric field and electric displacement vector, respectively, ρ is the mass density, r accounts for mass-related heat sources and q_i is the heat flux density. Moreover, in compliance with the micromechanical model to follow, the additive decomposition of total power $\dot{w}$ into reversible and irreversible parts $\dot{w}^{\text{rev}}$ and $\dot{w}^{\text{irr}}$ is introduced. Plugging equations (3) and (4) into equation (2) yields

$$\dot{u} = \sigma_{ij}\dot{\varepsilon}_{ij} + E_i\dot{D}_i + \rho r - q_{i,i}. \tag{5}$$

In order to evaluate the irreversibility and direction of energy transfer of the investigated processes, the rate of change of volume specific entropy $\dot{s}$ is considered. Splitting into an exchange and an irreversible part $\dot{s}^{\text{ex}}$ and $\dot{s}^{\text{irr}}$, respectively, yields:

$$\dot{s} = \dot{s}^{\text{ex}} + \dot{s}^{\text{irr}}. \tag{6}$$

Letting T denote the absolute thermodynamic temperature, for which $T > 0$ holds at all times, the former encompasses volumetric entropy sources $\rho r/T$ and an entropy flux across the boundary q_i/T associated with reversible heat transfer, while the latter quantifies changes of entropy due to dissipative power $\dot{w}^{\text{irr}}$ and irreversible heat transfer at finite temperature gradients $T_{,i}$, resulting in [18, 19]

$$\dot{s}^{\text{ex}} = \frac{\rho r}{T} - \left(\frac{q_i}{T}\right)_{,i}, \tag{7}$$

$$\dot{s}^{\text{irr}} = \frac{\dot{w}^{\text{irr}}}{T} - \frac{q_i T_{,i}}{T^2}. \tag{8}$$

Upon combination of equations (7) and (8) and multiplication with T, the relation

$$T\dot{s} = T(\dot{s}^{\text{ex}} + \dot{s}^{\text{irr}}) = \rho r - q_{i,i} + \dot{w}^{\text{irr}} = \dot{q} + \dot{w}^{\text{irr}} \tag{9}$$

is obtained, which is also referred to as local balance of entropy [20], revealing that the dissipative power $\dot{w}^{\text{irr}}$ is equivalent to a volumetric heat source. Inserting equation (9) into (5) and accounting for equation (3) provides alternative formulations of the above derived balance of power, i.e.

$$\begin{aligned} \dot{u} &= \sigma_{ij}\dot{\varepsilon}_{ij} + E_i\dot{D}_i - \dot{w}^{\text{irr}} + T\dot{s} = \dot{w} - \dot{w}^{\text{irr}} + T\dot{s} \\ &= \dot{w}^{\text{rev}} + T\dot{s}, \end{aligned} \tag{10}$$

where the endmost equation represents the rate formulation of the well-known Gibbs relation [18, 21]. The 2nd law of thermodynamics postulates that irreversible entropy rates must be non-negative at all times, i.e. it follows

$$T\dot{s}^{\text{irr}} = T(\dot{s} - \dot{s}^{\text{ex}}) = T\dot{s} - \rho r + q_{i,i} - \frac{q_i T_{,i}}{T} \geqslant 0, \tag{11}$$

implying irreversible processes always result in a production of entropy. This inequality may be rewritten on the basis of equation (8), introducing the dissipation function $\dot{\chi}$:

$$\dot{\chi} = T\dot{s}^{\text{irr}} = \dot{w}^{\text{irr}} - \frac{q_i T_{,i}}{T} \geqslant 0, \tag{12}$$

imposing restrictions on the directions of irreversible processes. Going beyond equation (12), Truesdell and Noll [19] argued in favor of an even more rigorous formulation, claiming that each of the terms involved independently have to be non-negative:

$$\dot{w}^{\mathrm{irr}} \geqslant 0 \quad \text{and} \quad -\frac{q_i T_{,i}}{T} \geqslant 0. \tag{13}$$

The first relation will be applied to prove the thermodynamic consistency of the constitutive model introduced in the subsequent sections.

2.2. Microphysical model of a tetragonal ferroelectric grain

While a ferroelectric material point consists of several grains, each grain exhibits a domain structure of $n = 1, \ldots, 6$ domains in which tetragonal unit cells are uniformly aligned. Accounting for this domain structure in the style of [22], volume fractions $\nu^{(n)}$ of the n domain species are chosen as internal variables, for which the following conservation condition hold, see [14]:

$$\sum_{n=1}^{6} \nu^{(n)} = 1, \quad \nu^{(n)} \in [\nu_{\min}, 1] \ \forall n. \tag{14}$$

The constant lower bound $\nu_{\min} \in (0, 1/N]$ prevents domain species from vanishing. In compliance with the additive decomposition of the total power in equation (3), total strains and electric displacements are likewise split into reversible and irreversible contributions:

$$\varepsilon_{ij} = \varepsilon_{ij}^{\mathrm{rev}} + \varepsilon_{ij}^{\mathrm{irr}}, \quad D_i = D_i^{\mathrm{rev}} + P_i^{\mathrm{irr}}. \tag{15}$$

The domain volume fractions have an impact on both the averaged material properties of the grain, see section 2.3, and the grain's irreversible strain and polarization in terms of weighted sums [23]

$$\varepsilon_{ij}^{\mathrm{irr}}(\nu^{(n)}) = \sum_{n=1}^{6} \varepsilon_{ij}^{\mathrm{sp}(n)} \nu^{(n)},$$

$$P_i^{\mathrm{irr}}(\nu^{(n)}) = \sum_{n=1}^{6} P_i^{\mathrm{sp}(n)} \nu^{(n)}, \tag{16}$$

where $\varepsilon_{ij}^{\mathrm{sp}(n)}$ describes the spontaneous strain of transition from cubic to tetragonal phases and $P_i^{\mathrm{sp}(n)}$ denotes the spontaneous polarization. While domain species with opposite orientations may basically exhibit identical and reverse states of spontaneous strain and polarization, respectively, the six internal variables develop independently. Consequently, an unpolarized

state of a grain prevails if all volume fractions are identical, i.e. $\nu^{(n)} = \frac{1}{6} \ \forall n$. Ultimately, following the procedure suggested by Maugin and Muschik [21], the internal power dissipated due to irreversible domain wall motion $\dot{w}^{\mathrm{irr}}$ is identified as

$$\dot{w}^{\mathrm{irr}} = \sum_{n=1}^{6} G^{(n)} \dot{\nu}^{(n)}. \tag{17}$$

Here, $G^{(n)}$ represent the work conjugate forces of the internal variables, further on referred to as dissipative conjugate forces, which will be specified in section 2.4. Inserting equation (17) into the balance of power, equation (10), reveals the internal energy of a grain to be based on the independent variables $(\varepsilon_{ij}, D_i, \nu^{(n)}, s)$, whereupon the total time derivative of the internal energy is readily obtained:

$$\dot{u} = \left.\frac{\partial u}{\partial \varepsilon_{ij}}\right|_{D_i, \nu^{(n)}, s} \dot{\varepsilon}_{ij} + \left.\frac{\partial u}{\partial D_i}\right|_{\varepsilon_{ij}, \nu^{(n)}, s} \dot{D}_i$$

$$+ \sum_{n=1}^{6} \left.\frac{\partial u}{\partial \nu^{(n)}}\right|_{\varepsilon_{ij}, D_i, s} \dot{\nu}^{(n)} + \left.\frac{\partial u}{\partial s}\right|_{\varepsilon_{ij}, D_i, \nu^{(n)}} \dot{s}. \tag{18}$$

Equating coefficients of equations (10) and (18) provides the associated variables:

$$\sigma_{ij} = \left.\frac{\partial u}{\partial \varepsilon_{ij}}\right|_{D_i, \nu^{(n)}, s}, \qquad E_i = \left.\frac{\partial u}{\partial D_i}\right|_{\varepsilon_{ij}, \nu^{(n)}, s},$$

$$G^{(n)} = -\left.\frac{\partial u}{\partial \nu^{(n)}}\right|_{\varepsilon_{ij}, D_i, s}, \qquad T = \left.\frac{\partial u}{\partial s}\right|_{\varepsilon_{ij}, D_i, \nu^{(n)}}. \tag{19}$$

Equations (17) and (19) yield the thermodynamic closure condition

$$\left.\frac{\partial u}{\partial \nu^{(n)}}\right|_{\varepsilon_{ij}, D_i, s} + \left.\frac{\partial \dot{w}^{\mathrm{irr}}}{\partial \dot{\nu}^{(n)}}\right|_{G^{(n)}} = 0, \tag{20}$$

where $\dot{w}^{\mathrm{irr}}$ takes the role of a dissipation potential [16, 24].

2.3. Constitutive equations of ferroelectricity

The formulation of constitutive equations in terms of the internal energy density $u(\varepsilon_{ij}, D_i, \nu^{(n)}, s)$ is rather inconvenient in light of difficulties controlling the electric displacement D_i and specific entropy s in experiments. Consequently, replacement of D_i and s with the electric field E_i and temperature change $\theta = T - T_0$ as independent variables, with T_0 denoting a reference temperature, is performed by means of twofold Legendre-transformation, where convexity of u is presumed, ending up with the generalized specific electric enthalpy $h(\varepsilon_{ij}, E_i, \nu^{(n)}, \theta)$:

$$h(\varepsilon_{ij}, E_i, \nu^{(n)}, \theta) = u(\varepsilon_{ij}, D_i, \nu^{(n)}, s) - \left.\frac{\partial u}{\partial D_i}\right|_{\varepsilon_{ij}, \nu^{(n)}, s} D_i - \left.\frac{\partial u}{\partial s}\right|_{\varepsilon_{ij}, D_i, \nu^{(n)}} s = u - E_i D_i - Ts. \tag{21}$$

The total time derivative of equation (21) evaluates to

$$\dot{h} = \dot{u} - \dot{E}_i D_i - E_i \dot{D}_i - \dot{T}s - T\dot{s}$$
$$= \sigma_{ij}\dot{\varepsilon}_{ij} - D_i\dot{E}_i - \dot{w}^{\mathrm{irr}} - s\dot{\theta}. \qquad (22)$$

In connection with the total time derivative of the electric enthalpy density and equation (17), the associated variables are obtained as

$$\sigma_{ij} = \left.\frac{\partial h}{\partial \varepsilon_{ij}}\right|_{E_i,\nu^{(n)},\theta}, \qquad D_i = -\left.\frac{\partial h}{\partial E_i}\right|_{\varepsilon_{ij},\nu^{(n)},\theta},$$
$$G^{(n)} = -\left.\frac{\partial h}{\partial \nu^{(n)}}\right|_{\varepsilon_{ij},E_i,\theta}, \qquad s = -\left.\frac{\partial h}{\partial \theta}\right|_{\varepsilon_{ij},E_i,\nu^{(n)}}. \qquad (23)$$

In the case of the dissipative conjugate forces $G^{(n)}$, no distinction has to be made between the underlying potentials

$u(\varepsilon_{ij}, D_i, \nu^{(n)}, s)$ or $h(\varepsilon_{ij}, E_i, \nu^{(n)}, \theta)$, as long as the dissipative power $\dot{w}^{\mathrm{irr}}$ according to equation (17) is considered to be valid in both cases as well:

$$\sum_{n=1}^{6} G^{(n)}\dot{\nu}^{(n)} = -\sum_{n=1}^{6}\left.\frac{\partial u}{\partial \nu^{(n)}}\right|_{\varepsilon_{ij},D_i,s}\dot{\nu}^{(n)}$$
$$= -\sum_{n=1}^{6}\left.\frac{\partial h}{\partial \nu^{(n)}}\right|_{\varepsilon_{ij},E_i,\theta}\dot{\nu}^{(n)} = \dot{w}^{\mathrm{irr}}. \qquad (24)$$

The following formulation of the specific thermodynamic potential h provides the entire information of a ferroelectric grain accounting for elastic, dielectric, piezoelectric and thermal properties as well as irreversible contributions governed by the internal variables $\nu^{(n)}$

$$h(\varepsilon_{ij}, E_i, \nu^{(n)}, \theta) = \frac{1}{2}\left(C_{ijkl}\left(\nu^{(n)}\right)\left[\varepsilon_{ij} - \varepsilon_{ij}^{\mathrm{irr}}\left(\nu^{(n)}, \theta\right)\right]\left[\varepsilon_{kl} - \varepsilon_{kl}^{\mathrm{irr}}\left(\nu^{(n)}, \theta\right)\right] - \kappa_{ij}\left(\nu^{(n)}\right)E_i E_j\right) - e_{ijk}\left(\nu^{(n)}\right)\left[\varepsilon_{ij} - \varepsilon_{ij}^{\mathrm{irr}}\left(\nu^{(n)}, \theta\right)\right]$$
$$E_k - \beta_{ij}\left(\nu^{(n)}\right)\left[\varepsilon_{ij} - \varepsilon_{ij}^{\mathrm{irr}}\left(\nu^{(n)}, \theta\right)\right]\theta - P_i^{\mathrm{irr}}\left(\nu^{(n)}, \theta\right)E_i - \rho c_v(\theta + T_0)\left[\ln\left(\frac{\theta}{T_0} + 1\right) - 1\right] - s_0\theta, \qquad (25)$$

where a specific reference entropy s_0 has been introduced. All material tensors, namely the elasticity tensor C_{ijkl}, the dielectric tensor κ_{ij}, the piezoelectric tensor e_{ijk} and the thermal coefficients β_{ij}, depend on the internal variables $\nu^{(n)}$ according to

$$C_{ijkl}(\nu^{(n)}) = \sum_{n=1}^{6} C_{ijkl}^{(n)}\nu^{(n)}, \quad \kappa_{ij}(\nu^{(n)}) = \sum_{n=1}^{6} \kappa_{ij}^{(n)}\nu^{(n)},$$
$$e_{ijk}(\nu^{(n)}) = \sum_{n=1}^{6} e_{ijk}^{(n)}\nu^{(n)}, \quad \beta_{ij}(\nu^{(n)}) = \sum_{n=1}^{6} \beta_{ij}^{(n)}\nu^{(n)}. \qquad (26)$$

The density ρ and specific heat c_v as scalar quantities are both independent of the domain species. Lattice parameters depending on temperature render the spontaneous polarization and strain functions of θ, i.e.,

$$P_i^{\mathrm{sp}(n)} = P_i^{\mathrm{sp}(n)}(\theta), \quad \varepsilon_{ij}^{\mathrm{sp}(n)} = \varepsilon_{ij}^{\mathrm{sp}(n)}(\theta), \qquad (27)$$

the former of which is referred to as pyroelectric effect [25]. Generally, both magnitudes decrease upon approaching the material's Curie temperature, ultimately vanishing at phase transition from tetragonal to cubic unit cells. An alternate way of addressing this phenomenon with regard to spontaneous polarization is the introduction of pyroelectric coefficients $k_i = \partial D_i/\partial\theta$, attributed to the change of spontaneous polarization with temperature. With data of $P^{\mathrm{sp}}(\theta)$ and $\varepsilon^{\mathrm{sp}}(\theta)$ being available for a relevant temperature range the approach according to equation (27) is pursued here. Piezoelectric, dielectric and elastic constants, on the other hand, are assumed to be less temperature-dependent in the range

of interest, thus they remain constant in the model. Finally, the ferroelectric constitutive equations are extracted from the potential equation (25) with equation (23):

$$\sigma_{ij}(\varepsilon_{ij}, E_i, \nu^{(n)}, \theta) = C_{ijkl}(\nu^{(n)})\left(\varepsilon_{kl} - \varepsilon_{kl}^{\mathrm{irr}}(\nu^{(n)}, \theta)\right)$$
$$- e_{ijk}(\nu^{(n)})E_k - \beta_{ij}(\nu^{(n)})\theta, \qquad (28)$$

$$D_i(\varepsilon_{ij}, E_i, \nu^{(n)}, \theta) = e_{ijk}(\nu^{(n)})\left(\varepsilon_{jk} - \varepsilon_{jk}^{\mathrm{irr}}(\nu^{(n)}, \theta)\right)$$
$$+ \kappa_{ij}(\nu^{(n)})E_j + P_i^{\mathrm{irr}}(\nu^{(n)}, \theta), \qquad (29)$$

$$s(\varepsilon_{ij}, E_i, \nu^{(n)}, \theta) = s_0 + \beta_{ij}(\nu^{(n)})\left(\varepsilon_{ij} - \varepsilon_{ij}^{\mathrm{irr}}(\nu^{(n)}, \theta)\right)$$
$$+ \rho c_v \ln\left(\frac{\theta}{T_0} + 1\right) + \sigma_{ij}(\varepsilon_{ij}, E_i, \nu^{(n)}, \theta)\left.\frac{\partial \varepsilon_{ij}^{\mathrm{irr}}(\nu^{(n)}, \theta)}{\partial \theta}\right|_{\nu^{(n)}}$$
$$+ E_i \left.\frac{\partial P_i^{\mathrm{irr}}(\nu^{(n)}, \theta)}{\partial \theta}\right|_{\nu^{(n)}}. \qquad (30)$$

The natural logarithm in equation (30) reflects the assumption of temperature-independent ρc_v, which is in accordance with what has been presumed for the other mesoscopic material coefficients. Per definition, the specific heat relates to the internal energy density as follows:

$$\rho c_v = \left.\frac{\partial u}{\partial T}\right|_{\varepsilon_{ij},D_i,\nu^{(n)}} = \mathrm{const.} \qquad (31)$$

Inserting equation (21) and accounting for equation (23) yields the relation

$$\rho c_v = T\frac{\partial s}{\partial T}\bigg|_{\varepsilon_{ij},E_i,\nu^{(n)}} \quad \Leftrightarrow \quad \frac{\partial s}{\partial T}\bigg|_{\varepsilon_{ij},E_i,\nu^{(n)}} = \frac{\rho c_v}{T}. \quad (32)$$

Considering an unpoled state of the material ($\varepsilon_{ij}^{\mathrm{irr}}, P_i^{\mathrm{irr}} = 0$) as well as $\varepsilon_{ij}, E_i = $ const. during the experimental measurement of the specific heat in order to capture solely the material's thermal properties without interference of effects such as pyroelectricity, the following is obtained upon plugging equation (30) into equation (32):

$$\frac{\partial s}{\partial T}\bigg|_{\varepsilon_{ij},E_i,\nu^{(n)}=1/6} = \frac{\mathrm{d}}{\mathrm{d}T}\left[\rho c_v \ln\left(\frac{\theta}{T_0}+1\right)\right] = \frac{\rho c_v}{T}. \quad (33)$$

Moreover, the terms including $\partial\varepsilon_{ij}^{\mathrm{irr}}/\partial\theta$ and $\partial P_i^{\mathrm{irr}}/\partial\theta$ account for further temperature-dependency, whereupon the Maxwell

relations are satisfied:

$$\frac{\partial s}{\partial \varepsilon_{ij}}\bigg|_{E_i,\nu^{(n)},\theta} = -\frac{\partial^2 h}{\partial \varepsilon_{ij}\partial\theta}\bigg|_{E_i,\nu^{(n)}} = -\frac{\partial^2 h}{\partial\theta\partial\varepsilon_{ij}}\bigg|_{E_i,\nu^{(n)}}$$
$$= -\frac{\partial\sigma_{ij}}{\partial\theta}\bigg|_{\varepsilon_{ij},E_i,\nu^{(n)}},$$
$$\frac{\partial s}{\partial E_i}\bigg|_{\varepsilon_{ij},\nu^{(n)},\theta} = -\frac{\partial^2 h}{\partial E_i\partial\theta}\bigg|_{\varepsilon_{ij},\nu^{(n)}} = -\frac{\partial^2 h}{\partial\theta\partial E_i}\bigg|_{\varepsilon_{ij},\nu^{(n)}}$$
$$= \frac{\partial D_i}{\partial\theta}\bigg|_{\varepsilon_{ij},E_i,\nu^{(n)}}. \quad (34)$$

2.4. Evolution of the internal variables: switching criterion

Application of equation (23) to the potential according to equation (25) yields the dissipative conjugate force:

$$G^{(n)}(\varepsilon_{ij},E_i,\nu^{(n)},\theta) = \sigma_{ij}\varepsilon_{ij}^{\mathrm{sp}(n)} + E_i P_i^{\mathrm{sp}(n)} - \frac{1}{2}\left[\varepsilon_{ij}-\varepsilon_{ij}^{\mathrm{irr}}\right]\left[\varepsilon_{kl}-\varepsilon_{kl}^{\mathrm{irr}}\right]\frac{\partial C_{ijkl}}{\partial\nu^{(n)}} + \frac{1}{2}E_i E_j\frac{\partial\kappa_{ij}}{\partial\nu^{(n)}} + \left[\varepsilon_{ij}-\varepsilon_{ij}^{\mathrm{irr}}\right]E_k\frac{\partial e_{ijk}}{\partial\nu^{(n)}} + \left[\varepsilon_{ij}-\varepsilon_{ij}^{\mathrm{irr}}\right]\theta\frac{\partial\beta_{ij}}{\partial\nu^{(n)}}$$
$$= \sigma_{ij}\varepsilon_{ij}^{\mathrm{sp}(n)} + E_i P_i^{\mathrm{sp}(n)} - h_{\mathrm{mat}}^{(n)}. \quad (35)$$

All terms including partial derivatives of material tensors with respect to $\nu^{(n)}$ are subsequently comprised in $h_{\mathrm{mat}}^{(n)}$, for which the weighted sum is likewise introduced on grain level:

$$h_{\mathrm{mat}} = \sum_{n=1}^{6} h_{\mathrm{mat}}^{(n)}\nu^{(n)}. \quad (36)$$

The dissipative conjugate force is usually incorporated in evolution laws of the internal variables, in this case an energetic switching criterion governing domain wall motion. However, $G^{(n)}$, as given by equation (35), cannot be used explicitly for a switching criterion, since no process direction is indicated in its formulation. Instead, the thermodynamic driving force $f^{(n\to k)}$ is introduced as follows, see [22, 26, 27]:

$$f^{(n\to k)} = G^{(k)} - G^{(n)} = -\frac{\partial h}{\partial\nu^{(k)}}\bigg|_{\varepsilon_{ij},E_i,\theta} + \frac{\partial h}{\partial\nu^{(n)}}\bigg|_{\varepsilon_{ij},E_i,\theta} \quad (37)$$
$$= \sigma_{ij}\Delta\varepsilon_{ij}^{\mathrm{sp}(n\to k)} + E_i\Delta P_i^{\mathrm{sp}(n\to k)} - \Delta h_{\mathrm{mat}}^{(n\to k)}. \quad (38)$$

The superscript $(n\to k)$ refers to switching from domain species n to k, e.g. the change of spontaneous strain evaluates to

$$\Delta\varepsilon_{ij}^{\mathrm{sp}(n\to k)} = \varepsilon_{ij}^{\mathrm{sp}(k)} - \varepsilon_{ij}^{\mathrm{sp}(n)}. \quad (39)$$

In equation (38) $f^{(n\to k)}$ represents the electromechanical volume specific work of switching. Furthermore, the volume flux of the nth domain species $\dot\nu^{(n)}$ is split into increasing

and decreasing contributions $\dot\nu^{(k\to n)}$ and $\dot\nu^{(n\to k)}$, which are summed over all domains [23]:

$$\dot\nu^{(n)} = \sum_{k=1}^{6}\left(\dot\nu^{(k\to n)} - \dot\nu^{(n\to k)}\right), \quad \dot\nu^{(k\to n)} \geqslant 0 \,\forall n,k = 1,\ldots,6. \quad (40)$$

Inserting equations (37) and (40) into equation (17), the dissipative power is rewritten:

$$\dot w^{\mathrm{irr}} = \sum_{n=1}^{6} G^{(n)}\dot\nu^{(n)} = \sum_{k=1}^{6}\sum_{n=1}^{6} f^{(n\to k)}\dot\nu^{(n\to k)}. \quad (41)$$

On the basis of the switching work $f^{(n\to k)}$, the evolution equation for switching of species n to k in a grain is formulated as energetic criterion in terms of [14]

$$\dot\nu^{(n\to k)} = \dot\nu_0\mathcal{H}\left(\frac{f^{(n\to k)}}{w_{\mathrm{crit}}^{(n\to k)}}-1\right)\mathcal{H}\left(\frac{f^{(n\to k)}}{f_{\mathrm{max}}^{(n\to k)}}-1\right), \quad (42)$$

where $\dot\nu_0$ is a model parameter and $\mathcal{H}$ denotes the Heaviside-function, taking the value 1 for semi-positive arguments and 0 otherwise. The first Heaviside-function ensures that for switching to take place, the critical work of switching $w_{\mathrm{crit}}^{(n\to k)}$ is achieved, which, for 90° or 180° switching processes of tetragonal ferroelectrics, reads [22, 28]

$$w_{\mathrm{crit}}^{(n\to k)} = \begin{cases} \sqrt{2}P^{\mathrm{sp}}E_{\mathrm{C}}, & \pm 90° \\ 2P^{\mathrm{sp}}E_{\mathrm{C}}, & 180° \end{cases}, \quad (43)$$

where E_C is the material's coercive field. In case of multiple switching variants meeting this criterion, the second Heaviside-function selects the process going along with maximal dissipation of energy $f_{\max}^{(n \to k)}$ given by

$$f_{\max}^{(n \to k)} = \max_{n,k=1,\ldots,6} \left\{ f^{(n \to k)} \;\middle|\; f^{(n \to k)} \geqslant w_{\text{crit}}^{(n \to k)} \right\}. \quad (44)$$

It should be noted that the differential equation (42) is not solved implicitly, but rather provides incremental evolutions of internal variables in a staggered manner.

On the one hand, switching is considered an arbitrarily fast process in the model, which in turn disregards its dynamic nature. On the other hand, quasistatic macroscopic processes are assumed mechanically as well as electrically, which means external loads are typically applied with frequencies below 10^2 Hz. In this context, τ_R is introduced as a characteristic relaxation time of the material, here the time required for switching, and τ_M as the characteristic process time, being inversely proportional to the frequency of external loads. Based on these two quantities, DEBORAH's number

$$De = \frac{\tau_R}{\tau_M} \quad (45)$$

quantifies closeness to thermodynamic equilibrium within the framework of rational thermodynamics [21], indicating the appropriateness of a quasistatic treatment in the case of $De \ll 1$, which is satisfied here.

Finally, the reversible and irreversible powers of a grain in equation (3) are identified by means of equations (16), (17), (35) and (36) as follows:

$$\dot{w}^{\text{irr}} = \sigma_{ij}\dot{\varepsilon}_{ij}^{\text{irr}} + E_i\dot{P}_i^{\text{irr}} - \dot{h}_{\text{mat}}, \quad (46)$$

$$\dot{w}^{\text{rev}} = \dot{w} - \dot{w}^{\text{irr}} = \sigma_{ij}\left(\dot{\varepsilon}_{ij} - \dot{\varepsilon}_{ij}^{\text{irr}}\right) + E_i\left(\dot{D}_i - \dot{P}_i^{\text{irr}}\right) + \dot{h}_{\text{mat}}$$
$$= \sigma_{ij}\dot{\varepsilon}_{ij}^{\text{rev}} + E_i\dot{D}_i^{\text{rev}} + \dot{h}_{\text{mat}}. \quad (47)$$

Apparently, the change of material properties due to domain wall motion $\dot{h}_{\text{mat}}$ contributes to both reversible and irreversible powers. Taking into account that according to equation (42) $f^{(n \to k)} \geqslant w_{\text{crit}}^{(n \to k)} > 0$ and $\dot{\nu}^{(n \to k)} \geqslant 0$ for all admissible switching processes, the thermodynamic consistency of the evolution law is proven by equations (13) and (41).

2.5. CM for meso–macro transition

A macroscopic representative volume element (RVE) is modeled to consist of $m = 1,\ldots,M$ randomly oriented grains. By means of equations (28)–(30), the constitutive equations of the mth grain read

$$\sigma_{ij}^{(m)} = C_{ijkl}^{(m)}\left(\varepsilon_{kl}^{(m)} - \varepsilon_{kl}^{\text{irr}(m)}\right) - e_{lij}^{(m)}E_l^{(m)} - \beta_{ij}^{(m)}\theta^{(m)}, \quad (48)$$

$$D_i^{(m)} = e_{ikl}^{(m)}\left(\varepsilon_{kl}^{(m)} - \varepsilon_{kl}^{\text{irr}(m)}\right) + \kappa_{ij}^{(m)}E_j^{(m)} + P_i^{\text{irr}(m)}, \quad (49)$$

$$s^{(m)} = s_0^{(m)} + \beta_{ij}^{(m)}\left(\varepsilon_{ij}^{(m)} - \varepsilon_{ij}^{\text{irr}(m)}\right) + \rho c_v \ln\left(\frac{\theta^{(m)}}{T_0} + 1\right)$$
$$+ \sigma_{ij}^{(m)}\frac{\partial \varepsilon_{ij}^{\text{irr}(m)}}{\partial \theta^{(m)}} + E_i^{(m)}\frac{\partial P_i^{\text{irr}(m)}}{\partial \theta^{(m)}}, \quad (50)$$

where ρc_v, as scalar material property, is independent of the grain orientation. In order to obtain macroscopic state variables describing the RVE, homogenization in terms of volume averaging over all grains is conducted. By doing so, all grains are assumed to be of equal size, rendering the associated variables to be

$$\langle \sigma_{ij} \rangle = \frac{1}{M}\sum_{m=1}^{M}\sigma_{ij}^{(m)}, \quad \langle D_i \rangle = \frac{1}{M}\sum_{m=1}^{M}D_i^{(m)}, \quad \langle s \rangle = \frac{1}{M}\sum_{m=1}^{M}s^{(m)}, \quad (51)$$

where angled brackets are introduced for macroscopic averaged quantities. With regard to the independent variables, beyond volume averaging a generalized Voigt-assumption is made, postulating strains, electric fields and temperatures to be uniform in the RVE, further on marked with an overbar:

$$\langle \varepsilon_{ij} \rangle = \frac{1}{M}\sum_{m=1}^{M}\varepsilon_{ij}^{(m)} = \varepsilon_{ij}^{(m)} = \overline{\varepsilon}_{ij}, \quad (52)$$

$$\langle E_i \rangle = \frac{1}{M}\sum_{m=1}^{M}E_i^{(m)} = E_i^{(m)} = \overline{E}_i, \quad (53)$$

$$\langle \theta \rangle = \frac{1}{M}\sum_{m=1}^{M}\theta^{(m)} = \theta^{(m)} = \overline{\theta}. \quad (54)$$

Inserting the constitutive equations (48)–(50) as well as the generalized Voigt-assumption, equations (52)–(54), into equation (51) yields

$$\langle \sigma_{ij} \rangle = \langle C_{ijkl} \rangle\overline{\varepsilon}_{kl} - \langle C_{ijkl}\varepsilon_{kl}^{\text{irr}} \rangle - \langle e_{lij} \rangle\overline{E}_l - \langle \beta_{ij} \rangle\overline{\theta}, \quad (55)$$

$$\langle D_i \rangle = \langle e_{ikl} \rangle\overline{\varepsilon}_{kl} - \langle e_{ikl}\varepsilon_{kl}^{\text{irr}} \rangle + \langle \kappa_{ij} \rangle\overline{E}_j + \langle P_i^{\text{irr}} \rangle, \quad (56)$$

$$\langle s \rangle = \langle s_0 \rangle + \langle \beta_{ij} \rangle\overline{\varepsilon}_{ij} - \langle \beta_{ij}\varepsilon_{ij}^{\text{irr}} \rangle$$
$$+ \rho c_v \ln\left(\frac{\overline{\theta}}{T_0} + 1\right) + \left\langle \sigma_{ij}\frac{\partial \varepsilon_{ij}^{\text{irr}}}{\partial \overline{\theta}} \right\rangle + \left\langle \overline{E}_i\frac{\partial P_i^{\text{irr}}}{\partial \overline{\theta}} \right\rangle, \quad (57)$$

where, e.g.

$$\langle C_{ijkl}\varepsilon_{kl}^{\text{irr}} \rangle = \frac{1}{M}\sum_{m=1}^{M}C_{ijkl}^{(m)}\varepsilon_{kl}^{\text{irr}(m)}. \quad (58)$$

Furthermore, prescribing macroscopic stresses and electric fields in terms of external loads, i.e. $\langle \sigma_{ij} \rangle = \sigma_{ij}^{\text{ext}}$ and $\overline{E}_i = E_i^{\text{ext}}$, allows for the determination of the strains $\overline{\varepsilon}_{ij}$ via inversion of equation (55),

$$\overline{\varepsilon}_{kl} = \varepsilon_{kl}^{(m)} = \langle C_{ijkl} \rangle^{-1}\left(\sigma_{ij}^{\text{ext}} + \langle C_{ijno}\varepsilon_{no}^{\text{irr}} \rangle + \langle e_{nij} \rangle E_n^{\text{ext}} + \langle \beta_{ij} \rangle\overline{\theta}\right), \quad (59)$$

which in turn provides the individual stresses of each grain from equation (48), comprising both external loads and residual stresses due to intergranular interactions:

$$
\begin{aligned}
\sigma_{ij}^{(m)} = C_{ijkl}^{(m)} &\left(\langle C_{mnkl}\rangle^{-1} \left(\sigma_{mn}^{\text{ext}} + \langle C_{mnop}\varepsilon_{op}^{\text{irr}}\rangle + \langle e_{pmn}\rangle E_p^{\text{ext}}\right.\right. \\
&\left.\left.+ \langle\beta_{mn}\rangle\overline{\theta}\right)\right) - C_{ijkl}^{(m)}\varepsilon_{kl}^{\text{irr}(m)} - e_{lij}^{(m)}E_l^{\text{ext}} - \beta_{ij}^{(m)}\overline{\theta}. \quad (60)
\end{aligned}
$$

The electric displacement of a RVE is furthermore obtained from equations (56) and (59):

$$
\begin{aligned}
\langle D_i\rangle = \langle e_{ikl}\rangle &\left(\langle C_{mnkl}\rangle^{-1}\left(\sigma_{mn}^{\text{ext}} + \langle C_{mnop}\varepsilon_{op}^{\text{irr}}\rangle + \langle e_{pmn}\rangle E_p^{\text{ext}}\right.\right. \\
&\left.\left.+ \langle\beta_{mn}\rangle\overline{\theta}\right)\right) - \langle e_{ikl}\varepsilon_{kl}^{\text{irr}}\rangle + \langle\kappa_{ij}\rangle E_j^{\text{ext}} + \langle P_i^{\text{irr}}\rangle. \quad (61)
\end{aligned}
$$

The thermodynamic driving force, equation (38), is thus rewritten within the context of the CM, revealing stresses are involved on grain level according to equation (60) rather than just considering external stresses σ_{ij}^{ext} on the macroscopic level:

$$
f^{(n\to k)} = \sigma_{ij}^{(m)}\Delta\varepsilon_{ij}^{\text{sp}(n\to k)} + \overline{E}_i\Delta P_i^{\text{sp}(n\to k)} - \Delta h_{\text{mat}}^{(n\to k)}. \quad (62)
$$

By virtue of equation (62), microstructural evolution and grain interactions in terms of evolution of material tensors and residual stresses are incorporated in the switching criterion.

At last, equation (9) is exploited for the calculation of the temperature $\overline{T} = \overline{\theta} + T_0$ under adiabatic conditions ($\dot{q} = 0$):

$$
\overline{T}\langle\dot{s}\rangle = \langle\dot{w}^{\text{irr}}\rangle. \quad (63)
$$

Inserting equations (46) and (57), while further cancelling negligible contributions of thermal strains, changes of spontaneous strain and polarization with temperature as well as of dissipation by microstructural evolution of material tensors ($\dot{h}_{\text{mat}} = 0$), leads to

$$
\dot{\overline{\theta}} = \dot{\overline{T}} = \frac{\langle\sigma_{ij}\dot{\varepsilon}_{ij}^{\text{irr}}\rangle + \overline{E}_i\langle\dot{P}_i^{\text{irr}}\rangle}{\rho c_v}. \quad (64)
$$

In light of the quasistatic conditions of the CM, equation (64) is discretized in terms of nondimensional load steps N replacing the time t. Integration between N and $N + 1$ results in

$$
\begin{aligned}
&\overline{T}(N+1) - \overline{T}(N) \\
&= \frac{1}{\rho c_v}\int_N^{N+1}\left(\left\langle\sigma_{ij}(\tilde{N})\frac{\partial\varepsilon_{ij}^{\text{irr}}}{\partial\tilde{N}}\right\rangle + \overline{E}_i(\tilde{N})\left\langle\frac{\partial P_i^{\text{irr}}}{\partial\tilde{N}}\right\rangle\right)\mathrm{d}\tilde{N}.
\end{aligned}
$$
$$(65)$$

Application of the left RIEMANN sum to approximate the integral and replacing the derivatives by finite differences between the two load steps $(N+1)$ and N yields

$$
\overline{T}(N+1) \approx \overline{T}(N) + \frac{\langle\sigma_{ij}(N)(\varepsilon_{ij}^{\text{irr}}(N+1) - \varepsilon_{ij}^{\text{irr}}(N))\rangle + \overline{E}_i(N)\langle P_i^{\text{irr}}(N+1) - P_i^{\text{irr}}(N)\rangle}{\rho c_v}, \quad (66)
$$

where $\Delta N = (N+1) - N = 1$ has been taken into account.

2.6. Analysis of harvesting cycles

Simulation of the harvesting cycle presented in section 1 is conducted by prescription of the electromechanical loading scheme depicted in figures 1, 3 and 4, macroscopically assuming an uniaxial state of stress and electric field, which reads in Voigt-notation

$$
\langle\sigma_{ij}\rangle(N) = \sigma_{ij}^{\text{ext}}(N) = \begin{pmatrix}0, & 0, & \sigma_{33}^{\text{ext}}(N), & 0, & 0, & 0\end{pmatrix}^{\text{T}}, \quad (67)
$$

$$
\overline{E}_i(N) = E_i^{\text{ext}}(N) = \begin{pmatrix}0, & 0, & E_3^{\text{ext}}(N)\end{pmatrix}^{\text{T}}, \quad (68)
$$

where $N = N_s, \ldots, N_s + \mathcal{N}$ covers a load cycle consisting of $\mathcal{N}$ load steps. Having specified external loads in terms of equations (67) and (68), macroscopic strains $\overline{\varepsilon}_{ij}(N)$ and electric displacements $\langle D_i\rangle(N)$ are calculated by the CM according to equations (59) and (61).

In order to assess electromechanical works and dissipation over one load cycle, the energy balance, equations (5) and (10), respectively, is integrated in the limits of N_s and $N_e = N_s + \mathcal{N}$:

$$
\begin{aligned}
\int_{N_s}^{N_e}\mathrm{d}u &= \int_{N_s}^{N_e}\sigma_{ij}\mathrm{d}\varepsilon_{ij} + \int_{N_s}^{N_e}E_i\mathrm{d}D_i + \int_{N_s}^{N_e}\mathrm{d}q \\
&= \int_{N_s}^{N_e}\sigma_{ij}\mathrm{d}\varepsilon_{ij} + \int_{N_s}^{N_e}E_i\mathrm{d}D_i - \sum_{n=1}^{6}\int_{N_s}^{N_e}G^{(n)}\mathrm{d}\nu^{(n)} + \int_{N_s}^{N_e}T\mathrm{d}s \\
&= \int_{N_s}^{N_e}\mathrm{d}w^{\text{rev}} + \int_{N_s}^{N_e}T\mathrm{d}s. \quad (69)
\end{aligned}
$$

Denoting quantities with respect to one load cycle by 'lc', equation (69) allows for the specification of total mechanical and electrical works $w_{\text{m,lc}}$ and $w_{\text{el,lc}}$, heat q_{lc}, as well as irreversible and reversible works $w_{\text{lc}}^{\text{irr}}$ and $w_{\text{lc}}^{\text{rev}}$ as follows:

$$
\begin{aligned}
w_{\text{m,lc}} &= \int_{N_s}^{N_e}\sigma_{ij}\mathrm{d}\varepsilon_{ij}, \; w_{\text{el,lc}} = \int_{N_s}^{N_e}E_i\mathrm{d}D_i, \; q_{\text{lc}} = \int_{N_s}^{N_e}\mathrm{d}q, \\
w_{\text{lc}}^{\text{irr}} &= \sum_{n=1}^{6}\int_{N_s}^{N_e}G^{(n)}\mathrm{d}\nu^{(n)}, \; w_{\text{lc}}^{\text{rev}} = \int_{N_s}^{N_e}\mathrm{d}w^{\text{rev}}.
\end{aligned}
$$
$$(70)$$

In view of energy harvesting purposes, stationary cyclic processes are of special interest, which require all independent and dependent state variables to return to their initial values at the end of the load cycle:

$$\left.(\varepsilon_{ij}, D_i, \nu^{(n)}, s)\right|_{N_s} = \left.(\varepsilon_{ij}, D_i, \nu^{(n)}, s)\right|_{N_e} \tag{71}$$

$$\Rightarrow \quad \left.(\sigma_{ij}, E_i, G^{(n)}, T, u)\right|_{N_s} = \left.(\sigma_{ij}, E_i, G^{(n)}, T, u)\right|_{N_e}. \tag{72}$$

By means of equation (9) follows for an adiabatic load cycle ($\mathrm{d}q = 0 \,\forall N$), accompanied by switching processes ($\exists N$: $\mathrm{d}\nu^{(n)} \neq 0$),

$$s(N_e) - s(N_s) = \int_{N_s}^{N_e} \frac{\mathrm{d}s}{\mathrm{d}N}\mathrm{d}N = \int_{N_s}^{N_e} \underbrace{\frac{1}{T}\frac{\mathrm{d}w^{\mathrm{irr}}}{\mathrm{d}N}}_{\geqslant 0\,\forall N}\mathrm{d}N > 0, \tag{73}$$

i.e. a closed cyclic adiabatic process in which switching occurs does not exist. As a consequence, adiabatic harvesting cycles investigated here will go hand in hand with a continuous increase in entropy and temperature, respectively, ultimately preventing stationarity. However, due to the comparatively small rise of temperature associated with one single hysteresis loop with typical magnitudes of $10^{-1}\,\mathrm{K}$ observed in experiments and numerical simulations [29], two sequential load cycles may be regarded approximately identical, allowing for a quasistationary treatment.

For a stationary isothermal cycle ($\mathrm{d}T = 0 \,\forall N$, $s(N_s) = s(N_e)$), on the other hand, equation (9) provides the conclusion

$$\int_{N_s}^{N_e} T\mathrm{d}s = \oint T\mathrm{d}s = 0 \quad \Leftrightarrow \quad \oint \mathrm{d}q = -\oint \mathrm{d}w^{\mathrm{irr}} \leqslant 0. \tag{74}$$

Consequently, a net heat flux q_{lc} out of the system is required to compensate for the entropy production due to irreversible switching. In the case of an isentropic cycle ($\mathrm{d}s = 0 \,\forall N$), equation (9) yields

$$T\dot{s} = 0 \quad \Leftrightarrow \quad \dot{q} = -\dot{w}^{\mathrm{irr}} \leqslant 0 \tag{75}$$

at any time, which demands an even more rigorous, instantaneous compensation of the produced entropy. As a result of either stationary isothermal or isentropic cycles, the last equation of equation (69), accounting for equation (47), turns into

$$0 = \oint \mathrm{d}w^{\mathrm{rev}} = \oint \sigma_{ij}\mathrm{d}\varepsilon_{ij}^{\mathrm{rev}} + \oint E_i\mathrm{d}D_i^{\mathrm{rev}} + \sum_{n=1}^{6}\oint h_{\mathrm{mat}}^{(n)}\mathrm{d}\nu^{(n)}. \tag{76}$$

Within the special case of a reversible cyclic process ($\mathrm{d}\nu^{(n)} = 0 \,\forall N$), the loss-free conversion of mechanical to electrical work and vice versa, stemming only from the piezoelectric effect, is recovered from equation (76):

$$\oint \sigma_{ij}\mathrm{d}\varepsilon_{ij}^{\mathrm{rev}} = -\oint E_i\mathrm{d}D_i^{\mathrm{rev}}. \tag{77}$$

In order to approximate the integrals in equation (70), the trapezoidal rule is used between two adjacent loadsteps, while a transition from grain to RVE level is achieved via volume averaging. As an example, the mechanical work of one cycle turns into

$$w_{\mathrm{m,lc}}^{(m)} = \int_{N_s}^{N_e} \sigma_{ij}^{(m)}\mathrm{d}\varepsilon_{ij}^{(m)} \approx \sum_{k=N_s}^{N_e-1} \frac{\varepsilon_{ij}^{(m)}(k+1) - \varepsilon_{ij}^{(m)}(k)}{2}\left(\sigma_{ij}^{(m)}(k+1) + \sigma_{ij}^{(m)}(k)\right),$$

$$\langle w_{\mathrm{m}}\rangle_{,\mathrm{lc}} = \frac{1}{M}\sum_{m=1}^{M} w_{\mathrm{m,lc}}^{(m)} \approx \sum_{k=N_s}^{N_e-1} \frac{\overline{\varepsilon}_{ij}(k+1) - \overline{\varepsilon}_{ij}(k)}{2}\left(\sigma_{ij}^{\mathrm{ext}}(k+1) + \sigma_{ij}^{\mathrm{ext}}(k)\right). \tag{78}$$

Based on the macroscopic mechanical and electrical works, three figures of merit, previously introduced in Behlen *et al* [6], are given as

$$\eta = \frac{-\langle w_{\mathrm{el}}\rangle_{,\mathrm{lc}}}{\langle w_{\mathrm{m}}\rangle_{,\mathrm{lc}}}, \quad \eta^{\mathrm{irr}} = \frac{-\langle w_{\mathrm{el}}^{\mathrm{irr}}\rangle_{,\mathrm{lc}}}{\langle w_{\mathrm{m}}^{\mathrm{irr}}\rangle_{,\mathrm{lc}}}, \quad \varphi^{\mathrm{irr}} = \frac{\langle w_{\mathrm{el}}^{\mathrm{irr}}\rangle_{,\mathrm{lc}}}{\langle w_{\mathrm{el}}\rangle_{,\mathrm{lc}}}, \tag{79}$$

where η and η^{irr} are the total and irreversible efficiencies and φ^{irr} is the degree of irreversibility. While the former two indicate the quality of a cycle with respect to conversion of mechanical to electrical work, the latter quantifies the exploitation of the ferroelectric over the piezoelectric effect for electrical work output.

2.7. Optimization

Introducing the set of n parameters as parameter vector $(z_1, \ldots, z_n)^{\mathrm{T}} = \underline{z} \in \mathbb{R}^n$ and the set of k target functions as objective vector $(\xi_1(\underline{z}), \ldots, \xi_k(\underline{z}))^{\mathrm{T}} = \underline{\xi}(\underline{z}) \in \mathbb{R}^k$, a constrained multiobjective optimization problem seeking the maximum of the objective vector, i.e. simultaneous maximization of the target functions, is stated in the style of [30]

$$\max_{\underline{z} \in Z}\{\xi_1(\underline{z}), \ldots, \xi_k(\underline{z})\}, \quad Z = \{\underline{z} \in \mathbb{R}^n \mid \underline{g}(\underline{z}) \leqslant \underline{0}, \underline{h}(\underline{z}) = \underline{0}\}, \tag{80}$$

where Z is the feasible region restricting the allowable parameters in terms of inequality and equality constraints $\underline{g}(\underline{z})$ and $\underline{h}(\underline{z})$, respectively. A parameter vector $\underline{z}_1$ is defined to dominate another vector $\underline{z}_2$ if the following holds with respect to their

corresponding objective vectors

$$\forall i = 1, \ldots, k : \ \xi_i(\underline{z}_1) \geqslant \xi_i(\underline{z}_2) \quad \text{and}$$
$$\exists j \in \{1, \ldots, k\} : \ \xi_j(\underline{z}_1) > \xi_j(\underline{z}_2), \tag{81}$$

i.e., the objective vector $\underline{\xi}(\underline{z}_1)$ is not worse than $\underline{\xi}(\underline{z}_2)$ in any of its components and strictly better in at least one of them. Since the target functions are oftentimes conflicting, a single global optimum may not be found. Instead, the concept of Pareto optimal points is introduced in the following way: compared with a Pareto optimal point $\underline{\xi}(\underline{z}^*)$ with Pareto optimal parameters $\underline{z}^*$, no target function can be increased without diminishing at least one other target function. Therefore, $\underline{z}^*$ is not dominated by any other parameter vector. In light of equation (81), the set Z^* of Pareto optimal parameter vectors $\underline{z}^*$ is expressed mathematically as

$$Z^* = \{\underline{z}^* \in Z \mid \nexists \underline{z} \in Z, \underline{z} \neq \underline{z}^* : \ \forall i = 1, \ldots, k : \ \xi_i(\underline{z}) \geqslant \xi_i(\underline{z}^*),$$
$$\exists j \in \{1, \ldots, k\} : \ \xi_j(\underline{z}) > \xi_j(\underline{z}^*)\}, \tag{82}$$

where the image $\underline{\xi}(Z^*)$, consisting of all Pareto optimal points, represents the so-called Pareto front, whose identification is aimed at within problems of multiobjective optimization. In this work, the Pareto front of problems in the style of equation (80) is approximately determined with the aid of a multiobjective genetic algorithm (MOGA), which belongs to the category of evolutionary algorithms. Starting off with a population of random parameter vectors, the algorithm, inspired by the natural process of evolution, mutates and recombines parameters, evaluates the fitness of parameter vectors in terms of mutual domination, and finally forms the successive population consisting of the currently fittest individuals. This process is repeated until the fitness of the best individuals does not increase significantly anymore. The algorithm is implemented into the open source code Dakota [31].

3. Results

A cycle of reference (COR) is analyzed first in terms of re- and depolarization, efficiency and associated workflows as well as quality factors. Subsequently, the significance of the bias field to the repolarization process is investigated. Optimizations are eventually carried out at different ambient temperatures regarding the irreversible efficiency η^{irr} and the irreversible electric work output $\langle w_{\mathrm{el}}^{\mathrm{irr}} \rangle_{,\mathrm{lc}}$ of the cycle to maximize the cycle's exploitation of the ferroelastic effect.

3.1. COR

The electromechanical loading scheme of the COR is illustrated in figure 5 and constitutes a basis of the numerical simulations. Caloric aspects are disregarded at this point, presuming material related quantities at $\bar{T} = T_0 = 25\,^{\circ}\mathrm{C}$. A sinusoidal mechanical load with an amplitude σ_{A} is chosen, see figure 5(a). The electrical load is shown in figure 5(b) along with the states of polarization at selected points. Initially,

before the cycle starts, the material is pre-polarized. After pre-polarization, the harvesting field E_{H} remains constant, while the intensity of the compressive mechanical load increases. During this step, the material is depolarized, accompanied by harvesting of electric energy. While further increasing the mechanical compression to a maximum the electric field is reduced to the lower level of the bias field E_{B}, coming along with further depolarization. After this, the mechanical stress is smoothly relaxed while the electrical load remains constant in order to repolarize the material, driven by the residual stresses, see figure 2. Finally, the electric field is increased to the initial value E_{H} thus closing the cycle.

Figure 6 shows results of simulations based on the modeling framework outlined in section 2 and the electromechanical loading scheme of figure 5. The closed loops are obtained for the fourth cycle, confirming stationarity. The arrows indicate the direction of the process. While figure 6(a) shows the mechanical state diagram, where the gray area represents the energy input, figures 6(b) and (c) depict electrical state diagrams, where the gray areas represent the energy output. Obviously, a cycle with a loop like the red rectangle in figure 6(c) delivers the highest possible yield of electric energy, in this case focusing on the irreversible ferroelectric part, and is thus interpreted as a generalized Carnot-type cycle. In figure 6(d) the irreversible polarization is illustrated versus the mechanical stress. In order to further evaluate the COR, the quality-assessing quantities according to equation (79) are calculated from the fourth load cycle and listed in table 1. The functionality of the cycle is ensured by means of the combination of positive efficiency η and negative electric work output $\langle w_{\mathrm{el}} \rangle_{,\mathrm{lc}}$. In conjunction with the negative irreversible electrical work $\langle w_{\mathrm{el}}^{\mathrm{irr}} \rangle_{,\mathrm{lc}}$ as well as the high value of the degree of irreversibility φ^{irr}, the COR proves to be appropriate, meeting the fundamental idea of a ferroelectric energy harvester. The magnitude of φ^{irr} of approximately 66% illustrates that while around two-thirds of the total electrical work $\langle w_{\mathrm{el}} \rangle_{,\mathrm{lc}}$ is harvested from the ferroelectric effect, only one-third results from the linear piezoelectric effect. This implies that the cycle discussed so far is much better than the initial ideas of ferroelectric energy harvesting cycles discussed in [5] and [6].

Figure 7 shows results for the loading scheme of figure 5 in the style of figures 6(c) and (d), however, with a modified bias field $E_{\mathrm{B}} = 0$. Obviously, the electric energy output of the modified cycle is significantly lower than that with $E_{\mathrm{B}} > 0$. The bias field apparently has a major impact on the process of repolarization in supporting the residual stresses. Although the efficiency and merit of the modified cycle are reduced, see table 2, the process still works, delivering electric power with less technical effort. In order to maximize the ferroelectric efficiency, an optimization is required.

3.2. Optimized cycle

The COR is characterized by three distinctive process parameters E_{B}, E_{H} and σ_{A} as well as their sequence. In particular, the electric field was specified rather arbitrarily, merely based on the findings of the prior investigations from [6]. In order to
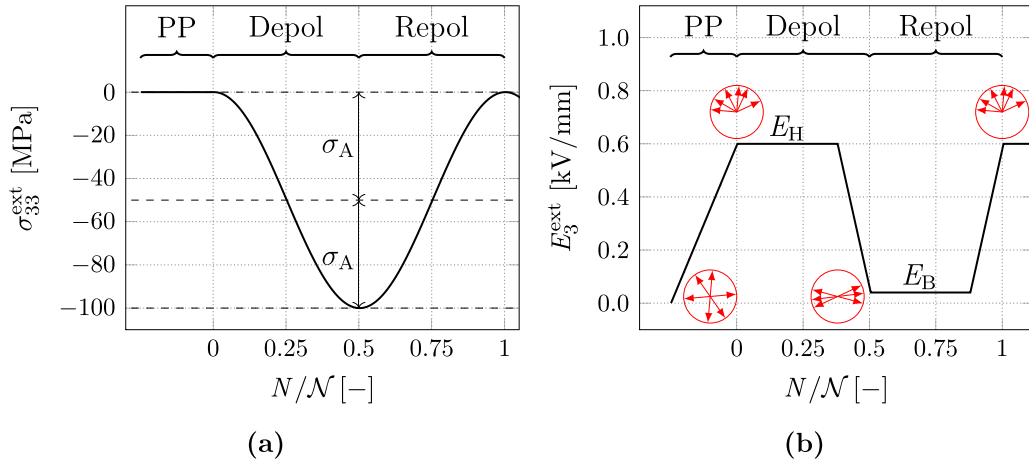
Figure 5. Electromechanical loading scheme of the cycle of reference; (a): mechanical stress $\langle \sigma_{33} \rangle = \sigma_{33}^{\text{ext}}$, (b): electric field $\overline{E}_3 = E_3^{\text{ext}}$ plotted vs. normalized load steps $N/\mathcal{N}$ of the first load cycle.

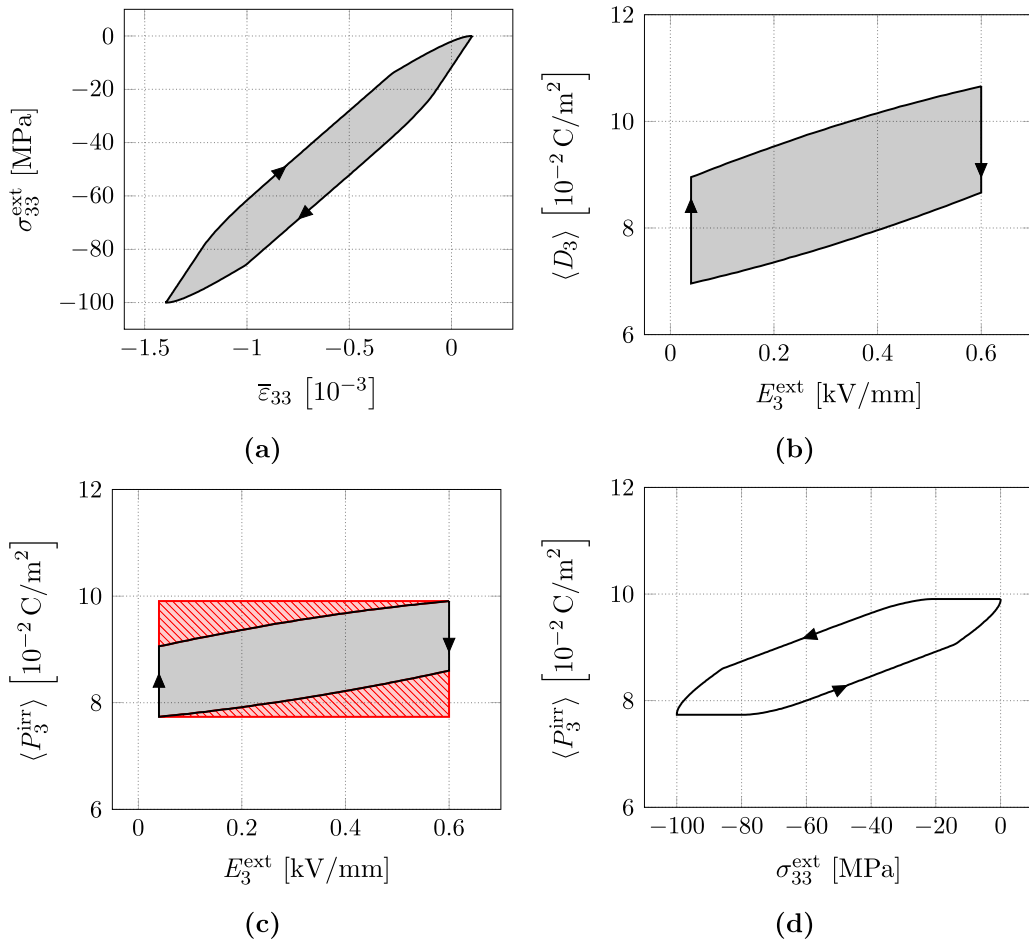**Figure 6.** Results of the fourth load cycle of the COR with loads according to figure 5; (a): stress σ_{33}^{ext} vs. strain $\overline{\varepsilon}_{33}$, (b): electric displacement $\langle D_3 \rangle$ vs. electric field E_3^{ext}, (c): irreversible polarization $\langle P_3^{\text{irr}} \rangle$ vs. electric field, hatched area represents additional electric output obtained in a Carnot-type cycle, (d): irreversible polarization $\langle P_3^{\text{irr}} \rangle$ vs. stress σ_{33}^{ext}.

gain a larger electrical power or to reduce the polarization loss, an improved concept of a harvesting process is introduced, see figure 8, where a uniform segmentation of the electrical load is adopted. The latter is characterized by eight significant points, E_{P1} to E_{P8}, all of which are allowed to take arbitrary values

within a prescribed range, see table 3. Furthermore, the compressive stress limit of $\sigma = -400\,\text{MPa}$ is in compliance with maximal loads applied in [32]. Within the optimization process, the intensity of the electric field will be identified explicitly for each of the eight points. While tensile stresses were

Table 1. Figures of merit of the COR.

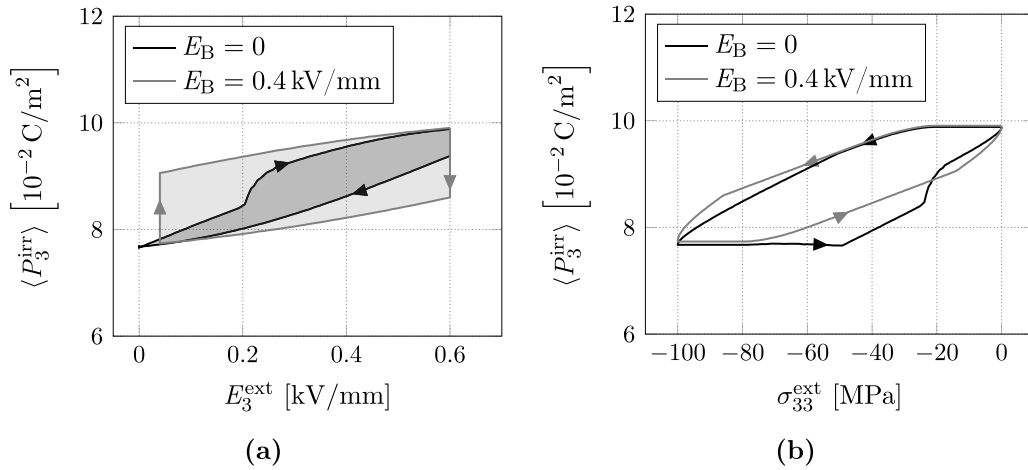| Quantity	$\langle w_{\mathrm{m}} \rangle_{,\mathrm{lc}}$	$\langle w_{\mathrm{el}} \rangle_{,\mathrm{lc}}$	$\langle w_{\mathrm{el}}^{\mathrm{irr}} \rangle_{,\mathrm{lc}}$	η	η^{irr}	φ^{irr}
Value	28.95	-11.99	-7.957	41.41	31.93	66.38
Unit	$\mathrm{kJ\,m^{-3}}$	$\mathrm{kJ\,m^{-3}}$	$\mathrm{kJ\,m^{-3}}$	%	%	%

Figure 7. Comparison of electrical state diagrams resulting from original loads of the cycle of reference according to figure 5 ($E_{\mathrm{B}} > 0$) to those with modified bias field $E_{\mathrm{B}} = 0$; irreversible polarization $\langle P_3^{\mathrm{irr}} \rangle$ vs. (a) electric field E_3^{ext} or (b) stress $\sigma_{33}^{\mathrm{ext}}$.

Table 2. Figures of merit of the COR with zero bias field.

Quantity	$\langle w_{\mathrm{m}} \rangle_{,\mathrm{lc}}$	$\langle w_{\mathrm{el}} \rangle_{,\mathrm{lc}}$	$\langle w_{\mathrm{el}}^{\mathrm{irr}} \rangle_{,\mathrm{lc}}$	η	η^{irr}	φ^{irr}
Value	25.11	-6.768	-3.789	26.96	17.11	55.98
Unit	$\mathrm{kJ\,m^{-3}}$	$\mathrm{kJ\,m^{-3}}$	$\mathrm{kJ\,m^{-3}}$	%	%	%
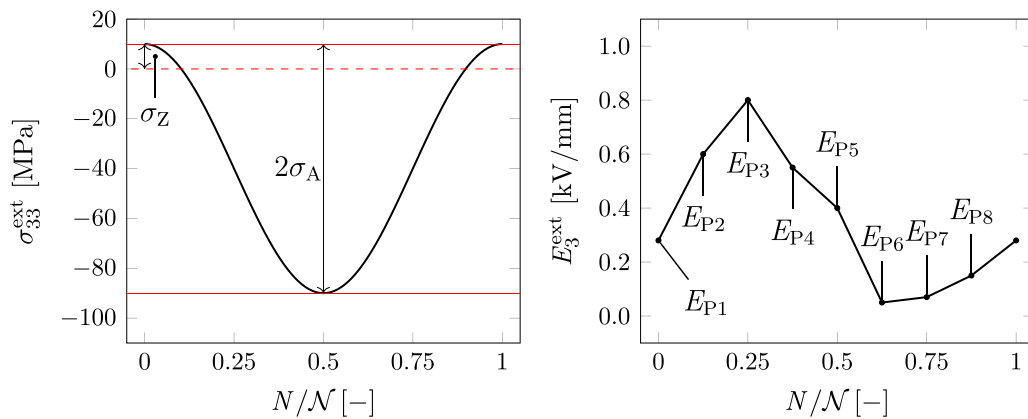
Figure 8. Electromechanical loading scheme parametrized in terms of ten process parameters $\sigma_{\mathrm{Z}}, \sigma_{\mathrm{A}}, E_{\mathrm{P1}}, \ldots, E_{\mathrm{P8}}$ with regard to an optimization.

Table 3. Constraints of the optimization in respect of the ten process parameters.

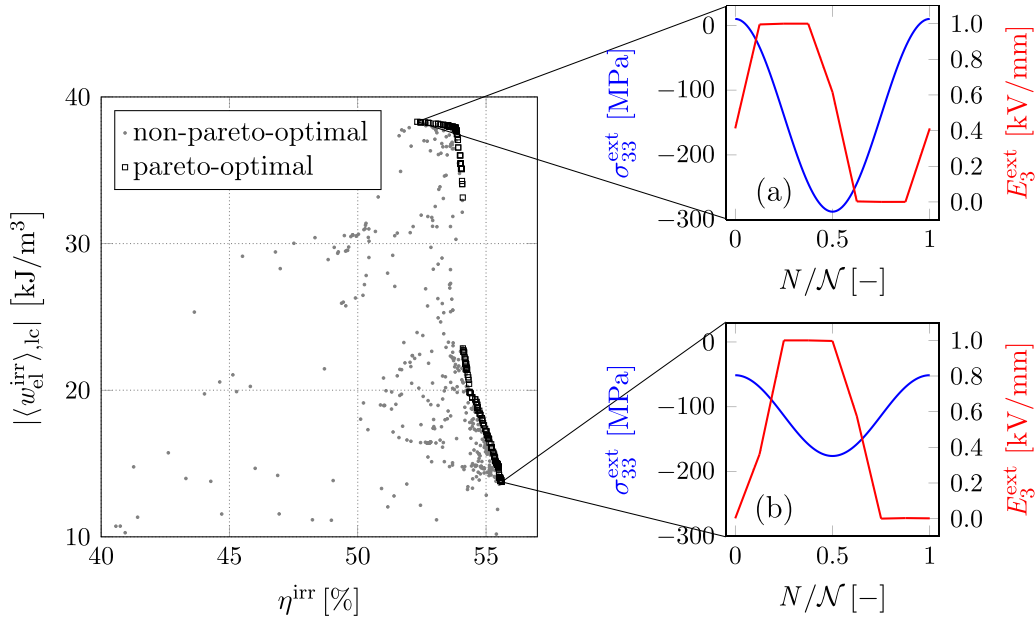| Parameter	Lower bound	Upper bound	Unit
σ_{Z}	10	-100	MPa
σ_{A}	0	150	
$E_{\mathrm{P1}}, \ldots, E_{\mathrm{P8}}$	0	1	$\mathrm{kV\,mm^{-1}}$

Figure 9. Results of the pareto-optimization with $\overline{T} = 25\,^{\circ}\mathrm{C}$ in terms of the absolute value of irreversible electric energy output $|\langle w_{\mathrm{el}}^{\mathrm{irr}} \rangle_{,\mathrm{lc}}|$ per cycle plotted versus the irreversible efficiency η^{irr}. The loading schemes corresponding to the two optimal points with maximal output (a) or efficiency (b) are provided on the right hand side.

deliberately avoided within the framework of the COR due to mechanical failure issues, a small magnitude of tensile stress is allowed for the improved cycle in view of a better energy yield.

For optimization, MOGA, see section 2.7, is used for seeking an optimal set of input or process parameters. The initial population consists of 50 sets of arbitrarily chosen parameters. Input parameters $\underline{z}$ and the constraint function $\underline{g}(\underline{z})$ follow from table 3, i.e.

$$\underline{z} = (E_{\mathrm{P1}}, \ldots, E_{\mathrm{P8}}, \sigma_{\mathrm{A}}, \sigma_{\mathrm{Z}})^{\mathrm{T}}, \tag{83}$$

$$\underline{g}(\underline{z}) = \left(\tilde{\underline{z}}^{\mathrm{T}} - 1\,\mathrm{kV/mm}\,\underline{I}^{\mathrm{T}}, \sigma_{\mathrm{A}} + 100\,\mathrm{MPa}, \sigma_{\mathrm{Z}} - 150\,\mathrm{MPa}, \right.$$
$$\left. -\tilde{\underline{z}}^{\mathrm{T}}, -\sigma_{\mathrm{A}}, 10\,\mathrm{MPa} - \sigma_{\mathrm{Z}} \right)^{\mathrm{T}}, \tag{84}$$

where $\tilde{\underline{z}} = (\underline{z}(1), \ldots, \underline{z}(8))^{\mathrm{T}}$ and $\underline{I} = (1, \ldots, 1)^{\mathrm{T}}$ with $\dim(\underline{I}) = \dim(\tilde{\underline{z}})$. Based on preliminary considerations on finding optimal cycles, it is postulated that the irreversible efficiency η^{irr} and the irreversible electric work output $\langle w_{\mathrm{el}}^{\mathrm{irr}} \rangle_{,\mathrm{lc}}$ are opposing targets, leading to the target function

$$\xi(\underline{z}) = (|\langle w_{\mathrm{el}}^{\mathrm{irr}} \rangle_{,\mathrm{lc}}|(\underline{z}), \eta^{\mathrm{irr}}(\underline{z}))^{\mathrm{T}}. \tag{85}$$

The relevant cycles are those which are pareto-optimal, meaning that a change in the parameters of the best cycles along the pareto front leads to a decrease of the irreversible efficiency while the irreversible work increases and vice versa.

Results from the optimization process are illustrated in figures 9–11. The irreversible electric work is plotted vs. the irreversible efficiency, whereat the optimizations were performed at different ambient temperatures from $25\,^{\circ}\mathrm{C}$ to $75\,^{\circ}\mathrm{C}$, based on the temperature-dependent properties

given by equations (88)–(90) and figure 14 in the appendix. Obviously, the electrical loading schemes of the selected pareto-optimal cycles with maximal electric output and efficiency, respectively, are similar for the three temperatures. In table 4, the results of figures 9–11 are summarized with regard to the electrical output and efficiency. First of all, it is concluded that the postulate of opposing targets actually holds. Furthermore, the pareto-optimal cycles are much better than the COR, compare table 1, in particular the irreversible electric work is increased by a factor of almost five. At $\overline{T} = 25\,^{\circ}\mathrm{C}$ the pareto–optimal cycle with the maximal efficiency, however, goes along with a remarkably low electrical energy output. Basically, the influence of temperature on both optimal efficiency and electric output is minor. It should be noted that analyses were done with an additional constant compressive load in perpendicular direction, however, not showing a noticeable effect on electric output or efficiency.

Table 5 shows the generated heat of all processes presented so far. The cycles having an optimal efficiency at a lower electric power output obviously produce less heat than those combining an optimal output with a lower efficiency. Considering that the heat production is proportional to the irreversible work associated with domain wall motion, this result is not unexpected. Furthermore, the magnitude of the dissipation may serve as a measure of the damage accumulation, thus allowing for a comparative assessment of life spans of the harvesting device subject to different process parameters.

Figure 12 shows the influence of the ambient temperature on both globally optimal cycles based on parameters identified at $\overline{T} = 25\,^{\circ}\mathrm{C}$, see figure 9. It should be mentioned that, for the sake of computational cost, the temperature has been prescribed, rather than calculated from self-heating being aware
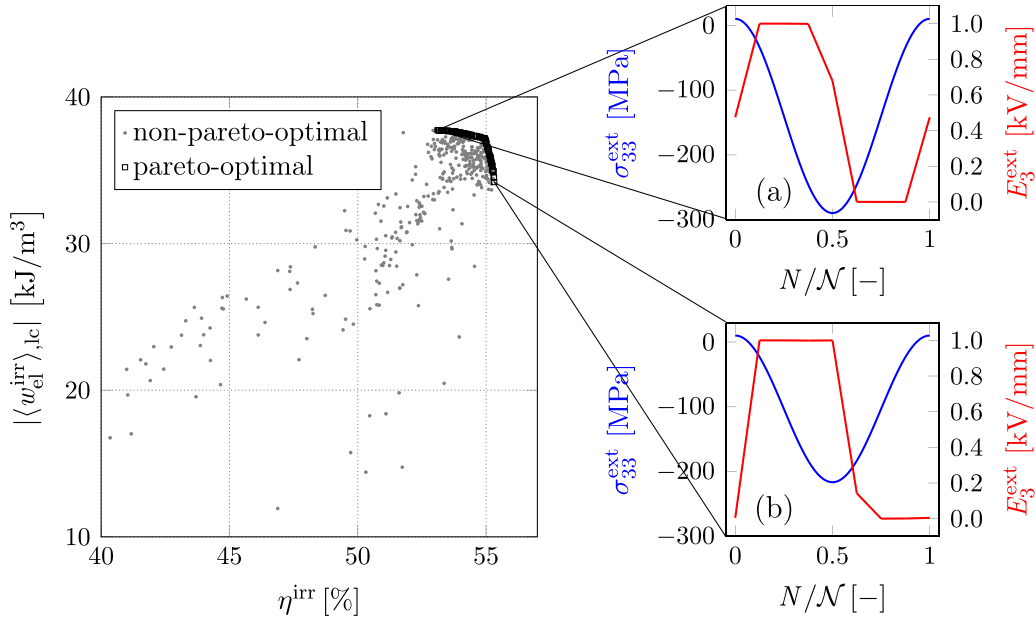
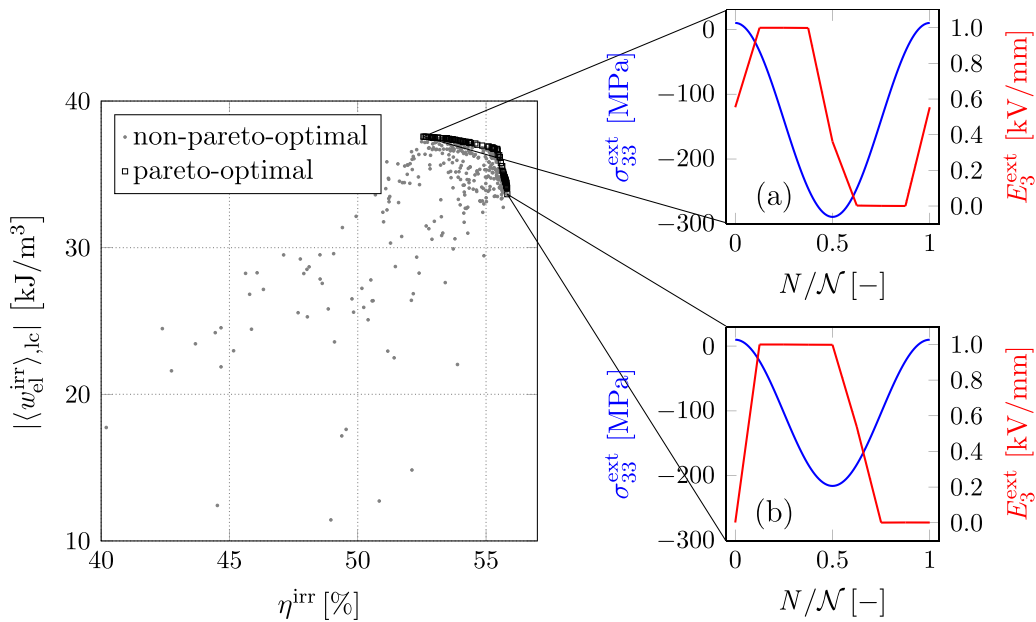**Figure 10.** Results of the pareto-optimization with $\overline{T} = 50\,°\mathrm{C}$ in the style of figure 9.

Figure 11. Results of the pareto-optimization with $\overline{T} = 75\,°\mathrm{C}$ in the style of figure 9.

Table 4. Results of the pareto-optimal cycles for temperatures $\overline{T} \in \{25\,°\mathrm{C}, 50\,°\mathrm{C}, 75\,°\mathrm{C}\}$, where (a) refers to the optimal output and (b) to the optimal efficiency.

Cycle	25(a)	25(b)	50(a)	50(b)	75(a)	75(b)
$\lvert\langle w^{\mathrm{irr}}_{\mathrm{el}}\rangle_{,\mathrm{lc}}\rvert\,[\mathrm{kJ\,m^{-3}}]$	38.31	13.75	37.75	34.19	37.57	33.65
$\eta^{\mathrm{irr}}\,(\%)$	52.32	55.62	53.12	55.32	52.56	55.83

that, e.g. the influence of thermal stress coefficients is thus neglected. The efficiency improves with increasing temperature and deteriorates drastically above 80 °C. While this applies to both globally pareto-optimized cycles, the temperature has a minor impact on the electrical power for cycles with an optimal irreversible electrical output, see figure 12(a). In contrast, the effect of temperature is larger for cycles with an optimal efficiency, see figure 12(a). In figure 13, the influence

Table 5. Produced heat per cycle of the COR and the pareto-optimal cycles for temperatures $\overline{T} \in \{25\,^{\circ}\text{C}, 50\,^{\circ}\text{C}, 75\,^{\circ}\text{C}\}$, where (a) refers to the optimal output and (b) to the optimal efficiency.
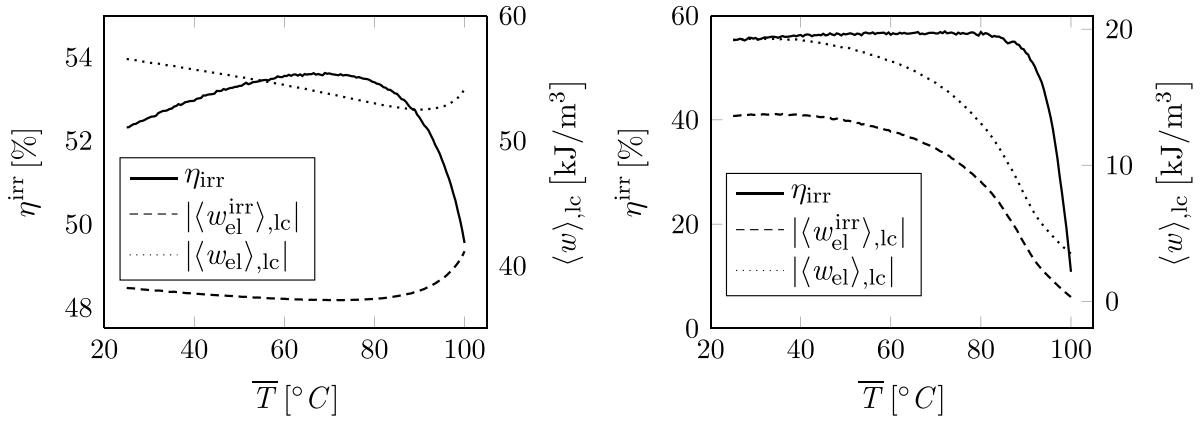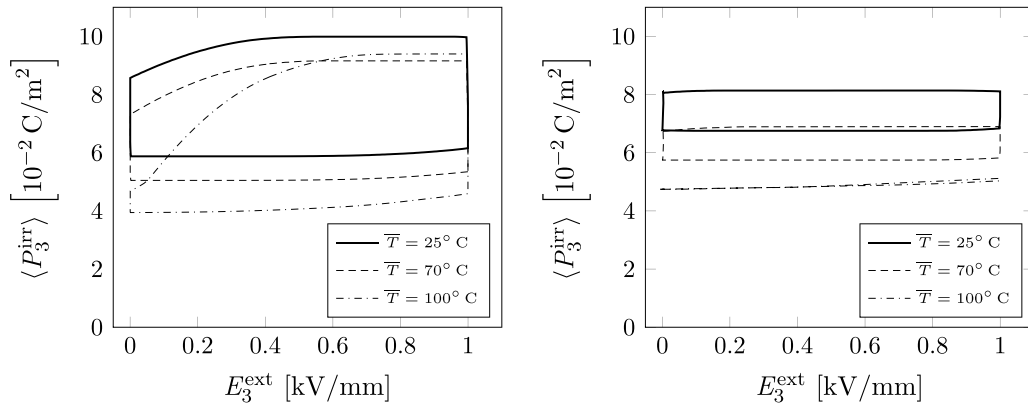
Cycle	COR	25(a)	25(b)	50(a)	50(b)	75(a)	75(b)
kJ m^{-3}	16.96	34.91	10.97	33.32	27.62	33.96	26.62

(a) Optimal cycle with respect to $|\langle w_{\text{el}}^{\text{irr}}\rangle_{,\text{lc}}|$

(b) Optimal cycle with respect to η^{irr}

Figure 12. figures of merit $\eta_{\text{irr}}, |\langle w_{\text{el}}^{\text{irr}}\rangle_{,\text{lc}}|$ and $|\langle w_{\text{el}}\rangle_{,\text{lc}}|$ versus temperature $\overline{T}$ with regard to the two globally optimal cycles based on process parameters identified at $\overline{T} = 25\,^{\circ}\text{C}$, see figure 9.

(a) Optimal cycle with respect to $|\langle w_{\text{el}}^{\text{irr}}\rangle_{,\text{lc}}|$

(b) Optimal cycle with respect to η^{irr}

Figure 13. Irreversible polarization vs. electric load over one loading cycle at three different temperatures for the two globally optimal cycles based on process parameters identified at $\overline{T} = 25\,^{\circ}\text{C}$, see figure 9.

of temperature on the loop of the polarization vs. electric field is shown, corresponding to the data in figure 12. Obviously, the impact is much larger on the cycles having an optimal efficiency than on those having an optimal output. One possible reason for the behavior at $\overline{T} < 100\,^{\circ}\text{C}$ might be the fact that cycles having an optimal electric output go along with larger mechanical loads than those having an optimal efficiency, resulting in a more efficient process of depolarization. At $\overline{T} = 100\,^{\circ}\text{C}$, the change of polarization virtually vanishes for the cycle having an optimal efficiency, no longer being appropriate. Obviously, the mechanical stress is not in the condition to depolarize against the electric field due to the considerable decrease of spontaneous strain at this temperature,

while the coercive field, as part of the switching threshold, is being much less reduced.

4. Conclusions

A scale-bridging approach of modeling ferroelectrics, including mutual nonlinear thermo-electromechanical couplings, has been applied successfully to investigate new concepts of energy harvesting. Exploiting domain switching, a comparatively large output of electric power is achieved in a cyclic process, dispensing with tensile stresses. These were formerly employed for depolarization and were known to

considerably reduce the life span of the harvester to the extent of non-operability. Allowing for a non-hazardous small magnitude of tensile stress in an optimized cycle further improves the electric power output. At room temperature, the latter, on the one hand, is largely reduced if aiming for maximum efficiency of energy conversion which, however, is not an issue at ambient temperatures of 50 °C and above. On the other hand, the efficiency of the process in terms of the ratio of electrical output to mechanical input is not crucial, the latter in general being available for free. Compared to a recently investigated cyclic process, where large compressive as well as tensile stresses were involved, the figures of merit could even be improved. The bias field, which supports the repolarization process and has to be imposed by a control unit, may basically be left out, however, leading to a reduction of electric output to almost half of the value with bias field. Finally, it should be mentioned that a pareto-optimization required approximately 10.000 simulations with individual parameter sets, which could only be achieved with reasonable computational cost due to the efficient multiscale approach based on the CM. An alternative formulation based on a mixed Voigt–Reuss approximation, where the electric displacement is assumed homogeneous in a polycrystalline RVE, additionally induces residual electric fields, which might take the role of an internal bias field in future investigations.

Data availability statement

The data that support the findings of this study are available upon reasonable request from the authors.

Appendix

In table 6, relevant quantities of the simulations are provided, whereupon $\Delta\nu_0$, representing a discrete change of domain volume, corresponds to the model parameter $\dot{\nu}_0$ introduced in equation (42) via $\dot{\nu}_0 = \Delta\nu_0/\tau_R$, with τ_R according to equation (45).

The difference between specific heat of crystalline solids measured at constant strain c_v and at constant stress c_p is negligible [33]. The values of ρ and c_v for BT at room temperature are [34]

$$\rho = 5840 \, \frac{\text{kg}}{\text{m}^3}, \tag{86}$$

$$c_v \approx c_p = 434 \, \frac{\text{J}}{\text{kg K}}. \tag{87}$$

Furthermore, the temperature-dependencies of the coercive field as well as spontaneous strain and polarization are based on experimental data [25, 35, 36]. In the simulations, they are approximated via third-degree polynomials fitted with the least-squares method, while room temperature values are matched with [14]:

$$E_C(T) = \left(-3.842 \cdot 10^{-2} \frac{T^3}{(°C)^3} + 5.877 \frac{T^2}{(°C)^2} \right.$$
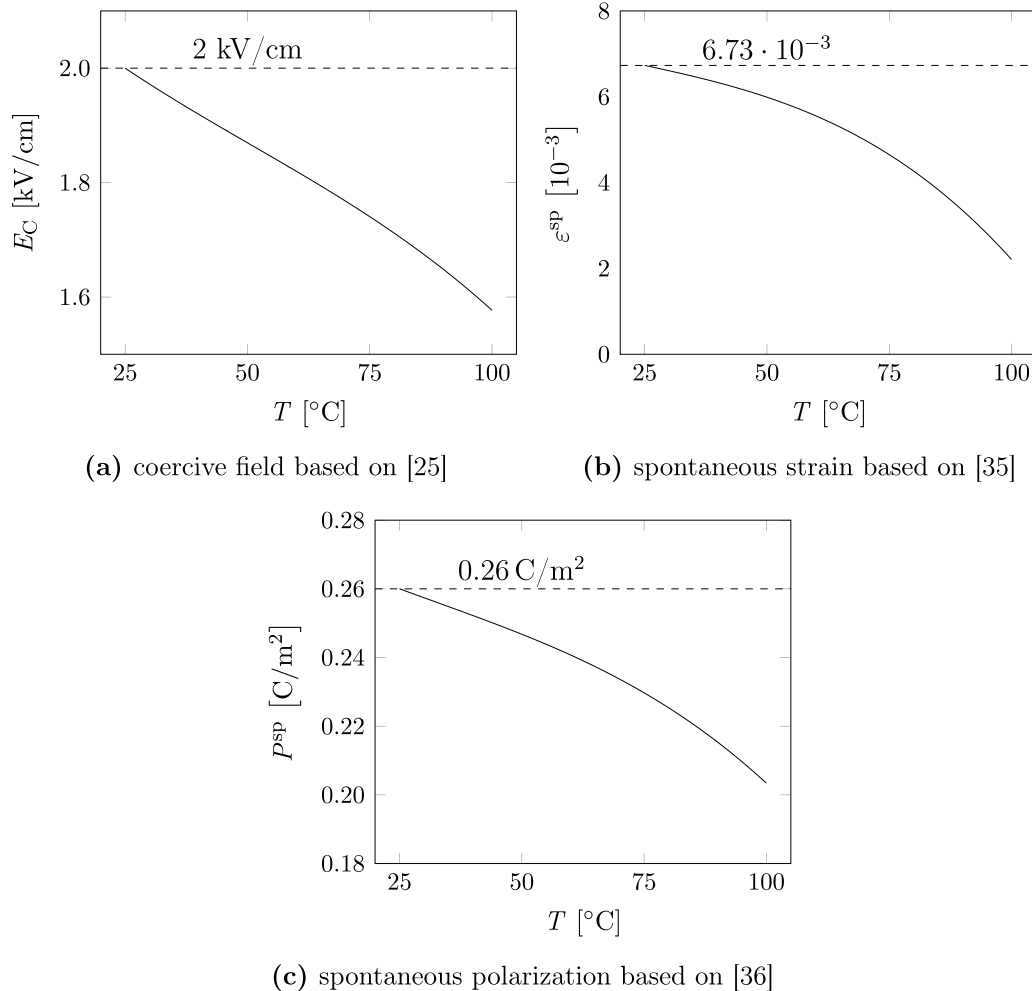$$\left. - 7.944 \cdot 10^2 \frac{T}{°C} + 216788 \right) \frac{V}{m}, \tag{88}$$

$$\varepsilon^{sp}(T) = -5.399 \cdot 10^{-9} \frac{T^3}{(°C)^3} + 3.313 \cdot 10^{-7} \frac{T^2}{(°C)^2}$$
$$- 3.086 \cdot 10^{-5} \frac{T}{°C} + 7.380 \cdot 10^{-3}, \tag{89}$$

$$P^{sp}(T) = \left(-5.808 \cdot 10^{-6} \frac{T^3}{(°C)^3} + 5.662 \cdot 10^{-4} \frac{T^2}{(°C)^2} \right.$$
$$\left. - 7.003 \cdot 10^{-2} \frac{T}{°C} + 27.490 \right) \frac{C}{m^2}. \tag{90}$$

In figure 14, the functions of equations (88)–(90) are visualized for a relevant range of temperature.

Table 6. Material constants of BT at room temperature (25 °C) and model parameters in compliance with [14].

Quantity	E_C	ε^{sp}	P^{sp}	$\Delta\nu_0$	ν_{min}	M
Value	2	0.0067	0.26	0.001	0.04	40
Unit	kV cm^{-1}	—	C m^{-2}	—	—	—

(a) coercive field based on [25]

(b) spontaneous strain based on [35]

(c) spontaneous polarization based on [36]

Figure 14. Temperature-dependency of the three ferroelectric material parameters of BT taken from literature, approximated via third-degree polynomials for a range of $T = 25\,°C$ to $T = 100\,°C$ and adjusted to the room temperature values of [14].

ORCID iDs

Andreas Warkentin ⃝ https://orcid.org/0000-0001-5277-6327
Lennart Behlen ⃝ https://orcid.org/0000-0002-2337-0050
Andreas Ricoeur ⃝ https://orcid.org/0000-0002-2193-1029

References

[1] Patel S, Chauhan A and Vaish R 2014 A technique for giant mechanical energy harvesting using ferroelectric/antiferroelectric materials *J. Appl. Phys.* **115** 084908
[2] Balakrishna A R and Huber J E 2016 Nanoscale domain patterns and a concept for an energy harvester *Smart Mater. Struct.* **25** 104001
[3] Wang D, Wang L and Melnik R 2017 Vibration energy harvesting based on stress-induced polarization switching: a phase field approach *Smart Mater. Struct.* **26** 065022
[4] Wang D, Melnik R and Wang L 2018 Material influence in newly proposed ferroelectric energy harvesters *J. Intell. Mater. Syst. Struct.* **29** 3305–16
[5] Kang W and Huber J E 2019 Prospects for energy harvesting using ferroelectric/ferroelastic switching *Smart Mater. Struct.* **28** 024002
[6] Behlen L, Warkentin A and Ricoeur A 2021 Exploiting ferroelectric and ferroelastic effects in piezoelectric energy harvesting: theoretical studies and parameter optimization *Smart Mater. Struct.* **30** 035031
[7] Kang W and Huber J E 2021 Energy harvesting based on compressive stress-induced ferroelectric/ferroelastic switching in polycrystalline ferroelectric materials *Cell Rep. Phys. Sci.* **3** 100707
[8] Kang W, Chang L and Huber J 2022 Investigation of mechanical energy harvesting cycles using ferroelectric/ferroelastic switching *Nano Energy* **93** 106862

[9] Cook-Chennault K A, Thambi N and Sastry A M 2008 Powering MEMS portable devices-a review of non-regenerative and regenerative power supply systems with special emphasis on piezoelectric energy harvesting systems *Smart Mater. Struct.* **17** 043001

[10] Wei C and Jing X 2017 A comprehensive review on vibration energy harvesting: modelling and realization *Renew. Sust. Energy Rev.* **74** 1–18

[11] Safaei M, Sodano H A and Anton S R 2019 A review of energy harvesting using piezoelectric materials: state-of-the-art a decade later (2008–2018) *Smart Mater. Struct.* **28** 113001

[12] Priya S *et al* 2019 A review on piezoelectric energy harvesting: materials, methods and circuits *Energy Harvest. Syst.* **4** 3–39

[13] Williams C B and Yates R B 1996 Analysis of a micro-electric generator for microsystems *Sens. Actuators* A **52** 8–11

[14] Lange S and Ricoeur A 2022 Multiscale modeling of ferroelectrics with stochastic grain size distribution *J. Intell. Mater. Syst. Struct.* **33** 1773–86

[15] Lange S and Ricoeur A 2015 A condensed microelectromechanical approach for modeling tetragonal ferroelectrics *Int. J. Solids Struct.* **54** 100–10

[16] Ricoeur A and Lange S 2019 Constitutive modeling of polycrystalline multiconstituent and multiphase ferroic materials based on a condensed approach *Arch. Appl. Mech.* **89** 973–94

[17] Parton V Z and Kudryavtsev B A 1988 *Electromagnetoelasticity: Piezoelectrics and Electrically Conductive Solids* (New York: Gordon and Breach Science Publishers)

[18] Malvern L E 1969 *Introduction to the Mechanics of a Continuous Medium* (*Prentice-Hall Series in Engineering of the Physical Sciences*) (Englewood Cliffs, NJ: Prentice-Hall)

[19] Truesdell C and Noll W 2004 *The Non-Linear Field Theories of Mechanics* (Berlin: Springer)

[20] Haupt P 2010 *Continuum Mechanics and Theory of Materials* (Berlin: Springer)

[21] Maugin G A and Muschik W 1994 Thermodynamics with internal variables. Part I. general concepts *J. Non-Equilib. Thermodyn.* **19** 217–49

[22] Huber J E, Fleck N A, Landis C M and McMeeking R M 1999 A constitutive model for ferroelectric polycrystals *J. Mech. Phys. Solids* **47** 1663–97

[23] Neumeister P 2011 Mikromechanische Modellierung morphotroper PZT-Keramiken *PhD Thesis* Technische Universität Dresden

[24] Biot M A 1965 *Mechanics of Incremental Deformations: Theory of Elasticity* (New York: Wiley)

[25] Bernard J, Cook W R and Jaffe H L 1971 *Piezoelectric Ceramics* (*Non-Metallic Solids*) (New York: Academic)

[26] Guin L and Kochmann D 2022 A phase-field model for ferroelectrics with general kinetics. Part I: model formulation (arXiv:2203.16479v1)

[27] Landis C M 2004 Non-linear constitutive modeling of ferroelectrics *Curr. Opin. Solid State Mater. Sci.* **8** 59–69

[28] Hwang S C, Lynch C S and McMeeking R M 1995 Ferroelectric/ferroelastic interactions and a polarization switching model *Acta Metall. Mater.* **43** 2073–84

[29] Warkentin A and Ricoeur A 2020 A semi-analytical scale bridging approach towards polycrystalline ferroelectrics with mutual nonlinear caloric-electromechanical couplings *Int. J. Solids Struct.* **200–201** 286–96

[30] Jürgen B, Kalyanmoy D, Kaisa M and Roman S 2008 *Multiobjective Optimization: Interactive and Evolutionary Approaches (Theoretical Computer Science and General Issues* LNTCS, vol 5252)

[31] Eldred M S, Dalbey K R, Bohnhoff W J, Adams B M, Swiler L P, Hough P D, Gay D M, Eddy J P and Haskell K H 2010 DAKOTA: a multilevel parallel object-oriented framework for design optimization, parameter estimation, uncertainty quantification, and sensitivity analysis. version 5.0, user's manual (https://doi.org/10.2172/991842)

[32] Barati M, Amini B, Segouin V, Daniel L, Chirani S A and Calloch S 2021 Investigation of self-heating and dissipative effects in ferroelectric ceramics subjected to compressive mechanical cyclic loading *Acta Mater.* **221** 117386

[33] Nye J F 1985 *Physical Properties of Crystals: Their Representation by Tensors and Matrices* (Oxford: Oxford Science Publications)

[34] Yi H 2004 Heat capacity, thermal conductivity and thermal expansion of barium titanate-based ceramics *Thermochim. Acta* **419** 135–41

[35] Kay H F 1948 Preparation and properties of crystals of barium titanate, $BaTiO_3$ *Acta Crystallogr.* **1** 229–37

[36] Merz W J 1953 Double hysteresis loop of $BaTiO_3$ at the Curie point *Phys. Rev.* **91** 513–17